In AGU-Wiley volume "*Crustal magmatic system evolution: Anatomy, architecture and physics-chemical processes*", edited by Matteo Masotta, Christoph Beier and Silvio Mollo. ISBN: 9781119564454

Trace element geothermometry and geospeedometry for cumulate rocks: Quantitative constraints on thermal and magmatic processes during igneous crust formation

Chenguang Sun

Department of Earth, Environmental and Planetary Sciences, Rice University
Houston, TX 77005, USA (Email: csun@rice.edu)

Keywords:
geospeedometry
geothermometry
mafic cumulate
crust formation

Abstract

Cumulate rocks record the magmatic and cooling processes during formation of Earth's igneous crust. Extracting the information of these two processes from mineral records, however, is often convoluted by various extents of diffusive resetting during cooling subsequent to main stages of crystallization. Accordingly, for cumulate rocks at diffusive closure, the apparent "equilibrium" temperatures derived from geothermometers are generally lower than the crystallization temperatures. Using analytical or numerical models, geospeedometers can extract cooling rates from the closure temperatures (or profiles) but only if the initial temperatures are determined independently. Here I summarize the general framework of geothermometry and geospeedometry from a trace element perspective. The Mg and REE-based exchange geothermometers for mafic cumulate rocks are reviewed as examples of the geothermometer design. Based on the observed differential diffusive closures of Mg and REE in oceanic gabbros, I outline a general resolution to uniquely determine the initial crystallization temperature and cooling rate of a cumulate rock. The basic idea is further demonstrated using the recently developed Mg-REE coupled geospeedometer for mafic cumulate rocks. Finally, I use the Hess Deep gabbros as a case study to show that this two-element coupled geospeedometer is particularly useful to delineate the igneous accretion and cooling styles during crust formation. This two-element (or multi-element) coupled approach outlined here can also be readily extended for decoding comprehensive thermal histories of other petrological systems at various geological settings or other rocky planetary bodies.

1. Introduction

Earth's crust is mainly composed of cumulate rocks, which are mafic beneath the oceans and vary from mafic to silicic at continents. Formation of Earth's igneous crusts generally involves generation, transport, emplacement, and differentiation of magmas that are primarily derived from partial melting of mantle and/or crustal materials (e.g., Nicolas et al., 1988; Phipps Morgan & Chen, 1993; Quick & Denlinger, 1993; Bachmann & Huber, 2016). Through buoyancy-driven migration, these melts could transport shallower and build up magma bodies or chambers at crustal levels. In the cold crustal environment, these magma bodies/chambers (Fig. 1) gradually solidify and evolve through fractional crystallization, melt replenishment, magma mixing, wall-rock assimilation, and/or volcanic eruption (e.g., Hildreth, 1979; DePaolo, 1981; Bachmann & Bergantz, 2004; Spera & Bohrson, 2004; Wark et al., 2007; Lee et al., 2014; Edmonds et al., 2019; Maclennan, 2019). Depending on the styles of magma supply (e.g., singular, pulsive, or continuous) and cooling (e.g., conductive or convective), these crustal magma bodies/chambers may undergo various solidification paths generating evolved melts and crystalline cumulates with diverse compositions. In this context, cumulate rocks can provide continuous records of magma solidification as a unique tool for unraveling the magmatic and thermal histories during igneous crust formation at different tectonic settings.

Primary questions on magma chamber processes concern (1) the composition of parental and differentiated magmas, (2) the igneous accretion and melt emplacement for building the crustal magma body, and (3) the cooling style and crustal environment of the solidifying magma body. Conventional approaches to deciphering these questions mostly rely on the chemical and isotopic compositions of the cumulate rocks (e.g., McBirney, 2003; Ashwal et al., 2005; Tegner et al., 2009; VanTongeren & Mathez, 2013; Namur & Humphreys, 2018; Tecchiato et al., 2018; Veksler et al., 2018; S. H. Yang et al., 2019) as well as forward simulations of magma crystallization and cooling using petrological models (e.g., Spera & Bohrson, 2004; Bohrson et al., 2014; Lee et al., 2014) or high-temperature experiments (e.g., Green & Ringwood, 1968; Grove et al., 1982; Morse et al., 2004; Koepke et al., 2018). Given that most magma bodies are open to various extents of melt influx and wall-rock assimilation, petrological modeling

and experimental simulation of the magma chamber behaviors are complicated by the unknown compositions and temperatures of parental and influx melts. Major element compositions of cumulate minerals/rocks are often used as petrological indexes (e.g., Mg# = 100×Mg/(Mg+Fe), and An# = 100×Ca/(Ca+Na+K) in mole) to qualitatively track fractional crystallization of the magma chamber and replenishment of melts with distinct compositions (e.g., Cawthorn & Walraven, 1998; Ashwal et al., 2005; Tegner et al., 2009; VanTongeren & Mathez, 2013; S. H. Yang et al., 2019). When the residual magmas have significant interactions with crustal wall-rocks, the primitive melt influx may also be differentiable through changes in isotopic compositions of the cumulate rocks (e.g., DePaolo, 1985; Kruger, 2005). These conventional approaches have significantly improved our knowledge of magmatic processes but are inadequate to constrain the igneous accretion and cooling histories of the magma bodies.

Crystallization temperatures and cooling rates of cumulate rocks are the two fundamental variables to pinpoint the extents of solidification, melt influx events, cooling histories, and residence times of the crustal magma bodies/chambers. These two variables can be determined by geothermometers and geospeedometers that are calibrated based on the temperature-dependent chemical equilibrium and diffusion between coexisting phases (e.g., minerals or melts), respectively. Many thermometers have been developed to determine crystallization temperatures of minerals in silicate melts (e.g., Putirka, 2005, 2008; Mollo et al., 2011; Masotta et al., 2013; Waters & Lange, 2015), but without the knowledge of equilibrium melt compositions, these thermometers are invalid for cumulate rocks. Upon crystallization, the cumulate minerals undergo subsequent cooling and diffusive exchange with their surroundings (Fig. 1). The diffusive response to changes in temperature, although complicates the estimation of crystallization (or initial) temperatures through geothermometers, enables the quantitative extraction of thermal histories from rock records using geospeedometers. The major challenges to resolving the thermal and magmatic histories of cumulate rocks thus include (1) development of relevant geothermometers, (2) quantitative characterization of diffusion behaviors of the key elements used in the geothermometers, and ultimately (3) accurate extraction of the crystallization temperature and cooling rate from a given cumulate rock.

With recent advance in the studies of trace element partitioning and diffusion in minerals, here I provide a trace element approach towards a general resolution for the magmatic and cooling histories of cumulate rocks. This paper is organized as follows: I first introduce the advantages of the trace element approach to decoding thermal-magmatic processes from mineral records in Section 2, and then outline the theoretical bases, calibration methods, and implementations of trace element geothermometers and

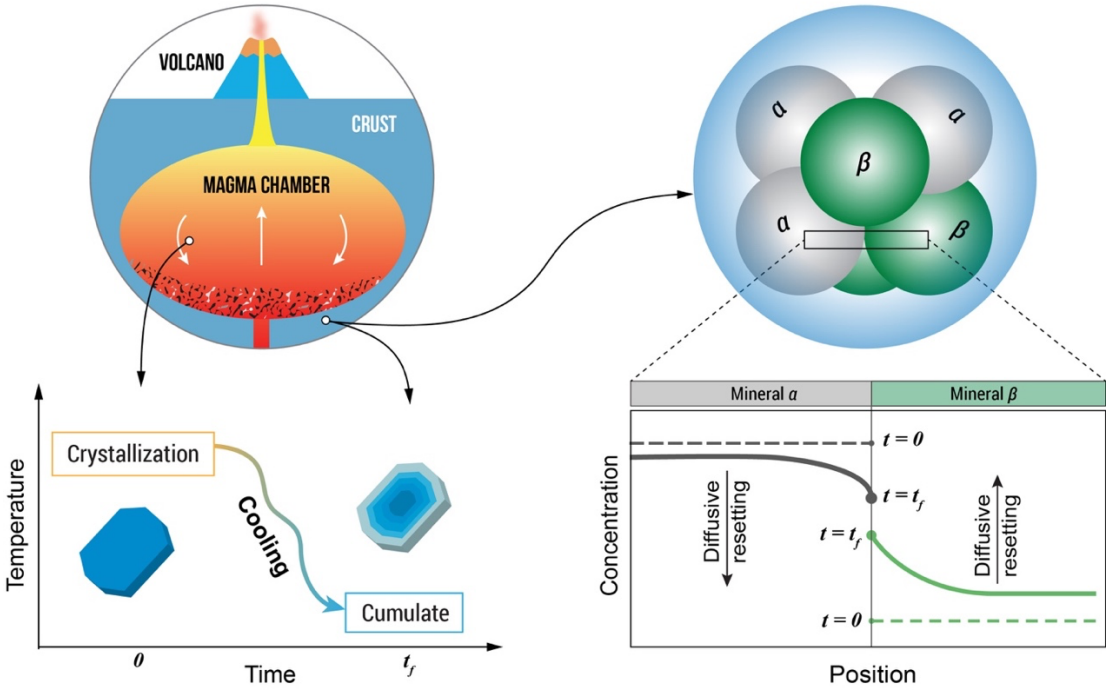

Figure 1. Schematic diagram showing the crystallization and cooling of cumulate rocks in a crustal magma chamber as well as the mineral responses to cooling after the main stages of crystallization. The magma chamber solidifies continuously in the cold crustal environment and evolves dynamically through melt replenishment, wall-rock assimilation, fractional crystallization, and perhaps volcanic eruption. These magmatic processes are recorded in cumulate rocks during solidification of the evolving magma chamber. Subsequent cooling, however, can alter the crystallization records in cumulate rocks to various extents by diffusive resetting.

geospeedometers in Sections 3 and 4. As a case study, in Section 5, I discuss the application of the Mg-REE coupled geospeedometer to oceanic gabbros and its implications for formation of fast-spreading lower oceanic crust. Using the recent developments of trace element geothermometry and geospeedometry for mafic cumulates, this paper aims to set up an integrated framework that could be extended for understanding comprehensive thermal histories of petrological systems in general.

2. A trace element perspective for decoding thermal-magmatic records in minerals

2.1. Equilibrium exchange

Partitioning describes the equilibrium distribution of a chemical species between two coexisting phases (α and β) and is quantitatively measured by the partition coefficient (K):

$$K_i = C_i^{\alpha} / C_i^{\beta} \ , \tag{1}$$

where C denotes the concentration of species i in each phase. Thermodynamically, the partition coefficient is derived from the equilibrium constant (K^{Θ}) for an exchange reaction between the two phases:

$$K^{\Theta} = \frac{a_i^{\alpha}}{a_i^{\beta}} = \frac{C_i^{\alpha}\gamma_i^{\alpha}}{C_i^{\beta}\gamma_i^{\beta}} = K_i \frac{\gamma_i^{\alpha}}{\gamma_i^{\beta}} \ , \tag{2}$$

where a and γ are the thermodynamic activity and activity coefficient of the chemical species, respectively. The equilibrium constant can be expressed as

$$\ln K^{\Theta} = -\frac{\Delta G}{RT} = -\frac{\Delta H}{RT} + \frac{\Delta S}{R} - \frac{P\Delta V}{RT} \ , \tag{3}$$

where ΔG, ΔH, ΔS, and ΔV are the changes of Gibbs free energy, enthalpy, entropy, and volume for the exchange reaction, respectively; R is the gas constant; T is temperature; and P is pressure.

According to equations (2–3), the thermodynamic expression of geothermometers can be generally written as

$$T = \frac{\Delta H + P\Delta V}{\Delta S - R\left(\ln K_i + \ln \gamma_i^{\alpha} - \ln \gamma_i^{\beta}\right)} \ . \tag{4}$$

Note that in equation (4), the partition coefficient defined by chemical concentration ratios (cf. equation (1)) is the only variable that can be directly measured from natural samples, while all others demand calibrations through systematic laboratory experiments. As major elements constitute the crystal lattice, their equilibrium exchange between different minerals involves other major elements (or components) to adjust the changes in crystal structure. For instance, Mg partitioning between coexisting mafic minerals (e.g., olivine, pyroxene and/or garnet) is generally considered coupling with Fe exchange (e.g., Ellis & Green, 1979; O'Neill & Wood, 1979). In addition, the activity coefficients of major elements, for their non-Henry's law behaviors, depend on their concentrations as well as other components in the minerals. With Henry's law behaviors, however, trace elements are expected to have activity coefficients independent of their concentrations, which practically reduces the complexity in geothermometer calibration.

2.2. Chemical diffusion

The intra-crystalline diffusive redistribution of an element is driven by the gradient of chemical potential. The corresponding diffusion coefficient (i.e., chemical diffusivity, D^*) is related to the intrinsic (i.e., tracer or self-) diffusion coefficient (D) through the following expression:

$$D^* = D\left(1 + \frac{\partial \ln \gamma}{\partial \ln C}\right) \ , \tag{5}$$

where $(1+\partial \ln\gamma/\partial \ln C)$ is the thermodynamic factor varying as a function of the concentration (C) and activity coefficient (γ) of the diffusing species (Darken, 1948). Distinct from the chemical diffusion, self- (or tracer-) diffusion takes place through spontaneous mixing driven by the gradient of isotopic ratios (or trace element abundance) in the crystal instead of the chemical potential gradient. Because of their Henry's law behaviors, trace elements have thermodynamic factors of unity, and thus their chemical diffusivities are effectively self- (or tracer-) diffusion coefficients. In light of these considerations, the experimentally determined D values for trace element cations can be directly used to model their diffusive exchanges in natural systems.

Because the equilibrium distribution of a major element between mineral pairs involves the exchange of additional major elements, the chemical diffusion of major elements in natural systems often behaves as a binary or multi-component diffusion process. Binary diffusion, also called interdiffusion, is used to describe diffusion in a binary system, while multi-component diffusion involves three or more components in the system (e.g., Lasaga, 1979; Watson & Baxter, 2007; Liang, 2010; Y. Zhang, 2010). For instance, Fe-Mg diffusion in olivine is an interdiffusion process (e.g., Chakraborty, 1997; Wang et al., 2004), given that olivine can be regarded as a binary solid solution of forsterite (Mg_2SiO_4) and fayalite (Fe_2SiO_4). Many other minerals are solid solutions of multiple components, such as the pyroxene solid solution composed of enstatite, ferrosilite, hedenbergite, and diopside components. For stoichiometry, diffusive redistribution of one major component in the mineral requires concurrent diffusive exchange of other components. Therefore, the chemical diffusion of a major element in binary or multi-component diffusion processes depends on the intrinsic diffusivity and thermodynamic behavior (i.e., activity coefficients) of this major element component as well as those of the coupling components in the system (e.g., Darken, 1948; Lasaga, 1979; Liang, 2010).

The coefficients of tracer and effective binary diffusion have been measured for major element cations in multi-component minerals (e.g., pyroxenes) under laboratory conditions; however, the two types of diffusivities could be

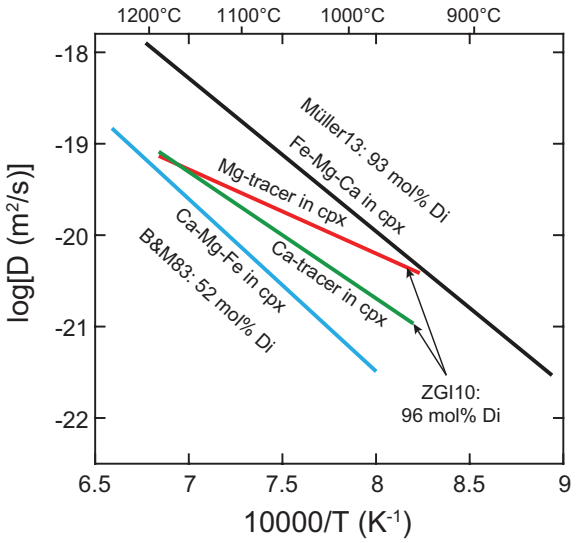

Figure 2. Comparison of diffusion data in clinopyroxene parallel to *c*-axis. The Mg and Ca tracer diffusivities were taken from Zhang et al. (2010; ZGI10) and measured for clinopyroxene (cpx) with 96 mol% diopside (Di) components. The Ca-(Mg+Fe) interdiffusion coefficients from Brady and McCallister (1983; B&M83) were determined for cpx with 52 mol% diopside components, while those from Müller et al. (2013) were measured for cpx with 93 mol% diopside components.

distinct from each other by up to about one order of magnitude in minerals with similar compositions, such as Ca and Mg in clinopyroxene with 93–96 mol% diopside (e.g., Cherniak & Dimanov, 2010; X. Zhang et al., 2010) (Fig. 2) . The significant differences are likely attributed to the non-Henry's law behaviors of major element components in the minerals in addition to the coupled diffusion of Ca-Mg-Fe in clinopyroxene. Therefore, tracer (or self-) diffusion coefficients should be used with great caution to model chemical diffusion of major elements in natural systems. It is also important to note that binary diffusion coefficients of an element couple may vary with the mineral composition. For example, the interdiffusion coefficients of Ca-(Mg+Fe) differ by about one and a half orders of magnitude in clinopyroxenes (Brady & McCallister, 1983; Müller et al., 2013) with different amounts of diopside components (52 vs. 93 mol%; Fig. 2). Given these complexities in major element diffusion, modeling trace element diffusion appears to be more straightforward to extract cooling histories from rock records.

3. Trace element-based geothermometry

As outlined in Section 2, the calibration of geothermometers is based on the partitioning of a chemical species or exchange of two coupled species between equilibrium phases. To provide an overview of trace element geothermometry, in this section I first summarize the theoretical bases of different trace element based geothermometers, briefly discuss the mechanism of trace element partitioning in minerals for thermometer calibration, and then review the trace element based geothermometers for mafic cumulate rocks.

3.1. Theoretical basis

According to equations (2–3), the partition (or exchange) coefficient (K) for a chemical species i between two phases (α and β) can be described by the thermodynamic expression:

$$\ln K_i = -\frac{\Delta G}{RT} - \ln\left(\frac{\gamma_i^\alpha}{\gamma_i^\beta}\right) = \frac{\Delta S}{R} - \frac{\Delta H + P\Delta V}{RT} - \ln\left(\frac{\gamma_i^\alpha}{\gamma_i^\beta}\right) . \quad (6)$$

For simplicity, equation (6) could also be written in a general form:

$$\ln K_i = A_i + \frac{B_i - f(P)}{T} , \quad (7)$$

where A and B are coefficients dependent on mineral major element compositions, and $f(P)$ is a pressure correction term for the exchange reaction. Although temperature in general is one of the intensive parameters controlling the exchange reaction, not all chemical exchanges are temperature sensitive. Hence, a major challenge in the design of a new geothermometer is to find the exchange reaction with a strong temperature dependence. Well-controlled laboratory experiments are subsequently required to calibrate A, B and $f(P)$ in equation (7). After tested by independent experiments or well-characterized field samples, equation (7) could then be turned into a geothermometer to determine temperatures of natural samples.

Trace element based geothermometers are usually calibrated using one exchange reaction or the partitioning of a single element between two coexisting minerals. For instance, the Ti-in-zircon and Ti-in-quartz thermometers are calibrated based on Ti partitioning in zircon and quartz, respectively, with coexisting rutile (e.g., Wark & Watson, 2006; Watson et al., 2006), and the Mg-in-plagioclase thermometer is based on Mg partitioning between plagioclase and clinopyroxene (Faak et al., 2013; Sun & Lissenberg, 2018a). A generic expression of single element based geothermometers follows the form of equation (4):

$$T = \frac{B_i - f(P)}{\ln K_i - A_i} . \quad (8)$$

Considering a group of geochemically similar elements (e.g., REE: rare earth elements), we can define their partition coefficients using the system of equations,

$$\ln\begin{bmatrix} K_1 \\ K_2 \\ \cdots \\ K_n \end{bmatrix} = \begin{bmatrix} A_1 \\ A_2 \\ \cdots \\ A_n \end{bmatrix} + \frac{1}{T}\begin{bmatrix} B_1 \\ B_2 \\ \cdots \\ B_n \end{bmatrix} - \frac{f(P)}{T} , \quad (9a)$$

where 1, 2, …, n denote the number of elements. Rearranged

in a linear form, equation (9a) can be written as:

$$\begin{bmatrix} B_1 \\ B_2 \\ \cdots \\ B_n \end{bmatrix} = T \begin{bmatrix} \ln K_1 - A_1 \\ \ln K_2 - A_2 \\ \cdots \\ \ln K_n - A_n \end{bmatrix} + f(P) \ . \tag{9b}$$

As presented in Sun & Liang (2017), equation (9b) can be written as a vector expression:

$$\vec{\mathrm{B}} = T\left(\ln\vec{\mathrm{K}} - \vec{\mathrm{A}}\right) + f(P) \ , \tag{10}$$

where $\vec{\mathrm{B}}$, $\vec{\mathrm{K}}$, and $\vec{\mathrm{A}}$ are column vectors of B_i, K_i, and A_i, respectively. In the (ln$K$−A) vs. B diagram (Fig. 3a), all elements in the group should define a straight line with the slope and intercept corresponding to the equilibrium temperature (T) and $f(P)$, respectively. Thus, equation (10) provides a new approach of geothermometer calibration, which has been implemented in orthopyroxene-clinopyroxene (Liang et al., 2013), garnet-clinopyroxene (Sun & Liang, 2015), and plagioclase-clinopyroxene systems (Sun & Liang, 2017).

It is important to note that the equilibrium temperature and pressure can be obtained simultaneously from equation (10) when their effects on the partition coefficients are both significant (cf. red line in Fig. 3a). Accurate determinate of pressures becomes difficult if the pressure effect is negligible or relatively small (i.e., $f(P) \approx 0$). In this case, $f(P)$ can be integrated into the coefficient B, and then equation (10) can be simplified as:

$$\vec{\mathrm{B}} = T\left(\ln\vec{\mathrm{K}} - \vec{\mathrm{A}}\right) \ . \tag{11}$$

Accordingly, all elements in the plot of (ln$K$−A) vs. B should define a straight line (cf. blue line in Fig. 3a) passing through the origin, the slope of which determines the equilibrium temperature. Distinct from the single element-based thermometers, this multi-element approach requires linear regression analyses of the partition coefficients of multiple elements. An obvious advantage of this multi-element approach is that it could make use of all the geochemically similar elements to determine temperatures (and pressures) with statistical confidence, even if some of the elements may appear as anomalies in the system due to alteration by later processes (e.g., metasomatism). When only one element is available, this multi-element approach recovers the single element-based geothermometer, which effectively determines the temperature by a straight line through this element and the origin (Fig. 3b). As this line is effectively defined by one element, accuracy of the temperature determination strongly relies on the analytical uncertainties of this element in the coexisting minerals.

3.2. Trace element partitioning

Trace elements are generally regarded as impurities substituting the major element cations in the crystal lattice site. As a major interest in petrology, trace element partitioning in various crystal-melt systems has been experimentally studied for magmatic processes (e.g., Gaetani & Grove, 1995; Tiepolo et al., 2007; van Westrenen & Draper, 2007; Le Roux et al., 2011; Wood & Blundy, 2013; Mollo et al., 2018; Sun, 2018; and references therein). Substitution of a trace element cation into the crystal lattice site (Fig. 4) needs to overcome the strain energy changes ($\Delta G_{\mathrm{strain}}$) in the crystal and other coexisting phase (χ; crystal or melt) in addition to the Gibbs free energy change (ΔG_0) for strain-free exchange of an ideal isovalent cation (Brice, 1975). The overall changes in Gibbs free energy can be described as:

$$\Delta G = \Delta G_0 - \Delta G_{\mathrm{strain}}^{\mathrm{crystal}} + \Delta G_{\mathrm{strain}}^{\chi} \ , \tag{12}$$

$$\Delta G_{\mathrm{strain}}^{\mathrm{crystal}} = 4\pi E N_A \left[\frac{r_0}{2}\left(r_0 - r_i\right)^2 - \frac{1}{3}\left(r_0 - r_i\right)^3\right] \ , \tag{13}$$

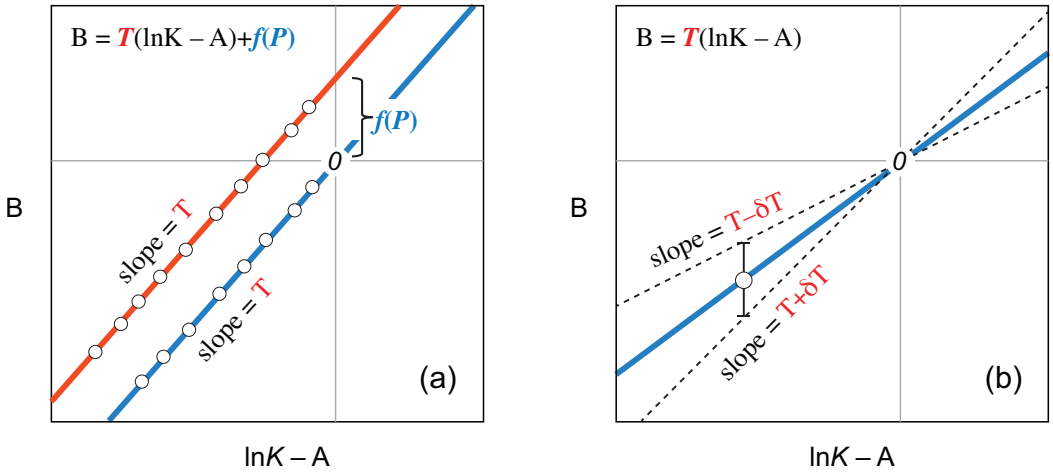

Figure 3. Schematic diagrams showing thermometers based on multiple elements (**a**) and a single element (**b**). The multi-element approach can potentially reduce the uncertainties of temperature calculations through statistical analysis of all relevant partitioning data.

where r_i is the ionic radius of the trace element cation (i) often taken from Shannon (1976) for the relevant coordination number, r_0 is the radius of an "ideal" or strain-free cation site in the crystal lattice, E is the apparent Young's modulus for the lattice site, and N_A is Avogadro's number.

When the crystal is coexisting with a melt, ΔG_{strain} of the melt can be neglected because the melt structure is much more relaxed than the crystal. Combining equation (6) with equations (12–13) derives a general expression to describe the partition coefficient of a trace element in this crystal-liquid system:

$$K_i^{\text{crystal/melt}} = K_0^{\text{crystal/melt}} \exp\left\{-\frac{4\pi E N_A}{RT}\left[\frac{r_0}{2}\left(r_0 - r_i\right)^2 - \frac{1}{3}\left(r_0 - r_i\right)^3\right]\right\}, \quad (14)$$

$$\ln K_0^{\text{crystal/melt}} = \frac{\Delta S_0}{R} - \frac{\Delta H_0 + P\Delta V_0}{RT} - \ln\left(\frac{\gamma_0^{\text{crystal}}}{\gamma_0^{\text{melt}}}\right), \quad (15)$$

where K_0 is the strain-free partition coefficient of the ideal cation and varies as a function of temperature, pressure, and composition. Equation (14) is sometimes called the Brice equation or lattice strain model (Blundy & Wood, 1994) for quantifying the parabolic relation between the crystal-melt partition coefficients of isovalent trace element cations and ionic radii in the Onuma diagram (Fig. 4). Through non-linear least-squares regression analyses, the three lattice strain parameters can be inverted from the crystal-melt partition coefficients of isovalent cations.

When the two coexisting phases are crystals (α and β), ΔG_{strain} has to be considered for both crystals (Fig. 4). Thus, in this mineral-mineral system, the partition coefficient of a trace element can be described through the following expression (Lee et al., 2007; Liang et al., 2013; Sun & Liang, 2014):

$$K_i^{\alpha/\beta} = K_0^{\alpha/\beta} \exp\left\{-\frac{4\pi E^{\alpha} N_A}{RT}\left[\frac{r_0^{\alpha}}{2}\left(r_0^{\alpha} - r_i\right)^2 - \frac{1}{3}\left(r_0^{\alpha} - r_i\right)^3\right] + \frac{4\pi E^{\beta} N_A}{RT}\left[\frac{r_0^{\beta}}{2}\left(r_0^{\beta} - r_i\right)^2 - \frac{1}{3}\left(r_0^{\beta} - r_i\right)^3\right]\right\}, \quad (16)$$

$$\ln K_0^{\alpha/\beta} = \ln\left(\frac{K_0^{\alpha/\text{melt}}}{K_0^{\beta/\text{melt}}}\right) = \frac{\Delta S_0^{\alpha/\beta}}{R} - \frac{\Delta H_0^{\alpha/\beta} + P\Delta V_0^{\alpha/\beta}}{RT} - \ln\left(\frac{\gamma_0^{\alpha}}{\gamma_0^{\beta}}\right). \quad (17)$$

As shown in equations (16–17), E and r_0 of the two crystals are identical to those in the two crystal-melt systems, while K_0 of the mineral-mineral system is equivalent to the ratios of K_0 in two crystal-melt systems. Although one may expect crystal-melt K_0 depending on melt compositions (i.e., γ_0^{melt}; equation

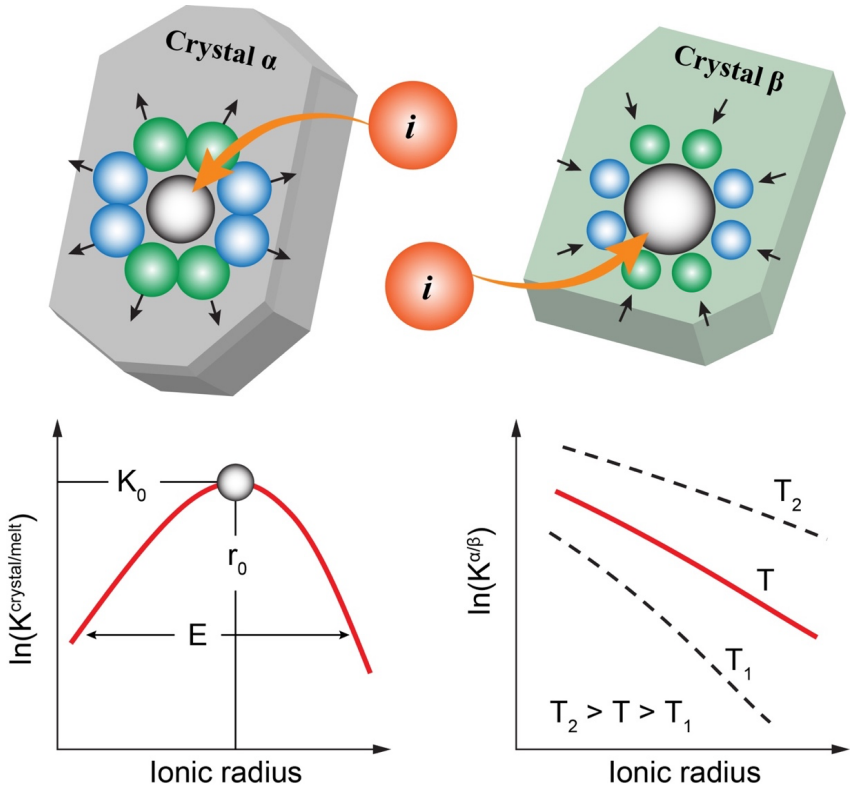

Figure 4. Cartoon drawings of trace element partitioning in crystals. The substitution of a trace element into the crystal lattice sites has to overcome the change of lattice strain energy, which depends on the relative size difference between the trace element cation and the ideal lattice site. In the crystal-melt system, partition coefficients of isovalent trace element cations follow a parabolic pattern in the Onuma diagram (Onuma et al., 1968) and are controlled by the three lattice strain parameters, D_0, E and r_0 (Modified after Sun, 2018). However, in the two-mineral system, partition coefficients of isovalent cations on the log scale generally manifest linear patterns with their ionic radii and vary systematically with the change of equilibrium temperatures.

(15)), the effect of melt composition, if any, can be cancelled out between $K_0^{\alpha/\mathrm{melt}}$ and $K_0^{\beta/\mathrm{melt}}$. For the calibration of single element-based geothermometers, it is not necessary to determine all six lattice strain parameters in equation (16). However, for the calibration of multi-element based geothermometers, understanding the systematic partitioning behaviors of isovalent cations is an important first step.

Given the non-linear trade-off between the six lattice strain parameters in equation (16), it is challenging to invert them directly from the measured partition coefficients between two coexisting minerals. Because these lattice strain parameters are effectively the same as those in the lattice strain model for crystal-melt systems (equation (14)), the experimentally determined mineral-melt partition coefficients can be used to invert the lattice strain parameters for individual minerals at a broad range of pressures and temperatures. The lattice strain parameters can then be parameterized as a function of temperature, pressure, and/or mineral composition. Substituting these models of lattice strain parameters into equation (16), one could obtain a generalized expression as a new geothermometer. Following this approach, previous studies have calibrated several multi-element geothermometers (Liang et al., 2013; Sun & Liang, 2015, 2017) using REE partitioning models for different mineral-melt systems (Sun & Liang, 2012, 2013a, 2013b; Yao et al., 2012; Sun et al., 2017).

3.3. Geothermometers for mafic cumulates

Plagioclase and clinopyroxene are the main rock-forming minerals co-crystallizing in mafic to intermediate magmas over an extended temperature interval (e.g., Grove & Bryan, 1983; Sisson & Grove, 1993). Thus, geothermometers for plagioclase-clinopyroxene systems are particularly useful to quantitatively constrain the equilibrium or crystallization temperatures of cumulate rocks. Recent studies have developed two types of geothermometers based on the exchange of multiple elements (REE; Sun & Liang, 2017) or a single element (Mg; Faak et al., 2013; Sun & Lissenberg, 2018a) between plagioclase and clinopyroxene. With the theoretic background outlined in Sections 3.1 and 3.2, here I briefly review the recently developed geothermometers for mafic cumulate rocks.

3.3.1. REE-in-plagioclase-clinopyroxene thermometer

The REE-in-plagioclase-clinopyroxene geothermometer (Sun & Liang, 2017) was established from the lattice strain models for clinopyroxene-melt (Sun & Liang, 2012) and plagioclase-melt systems (Sun et al., 2017). These lattice strain parameters were calibrated on 43 partitioning experiments for clinopyroxene-melt systems and 29 experiments for plagioclase-melt systems. The 43 clinopyroxene-melt partitioning experiments were conducted at 1042–1470 °C and 0.0001–4 GPa and crystalized clinopyroxene with Mg# of 54–100. The 29 plagioclase-melt partitioning experiments cover temperatures of 1127–1410°C, pressures of 0.0001–1.5 GPa, and a wide range of plagioclase compositions (An# = 41–98).

The lattice strain parameters for REE partitioning between clinopyroxene and melt can be described through the following expressions from Sun & Liang (2012):

$$\ln K_0^{\mathrm{cpx}} = -7.14 + \frac{7.19\times10^4}{RT} + 4.37X_{\mathrm{Al}}^{\mathrm{T,cpx}} + 1.98X_{\mathrm{Mg}}^{\mathrm{M2,cpx}} - 0.91X_{\mathrm{H_2O}}^{\mathrm{melt}} \quad (18)$$

$$r_0^{\mathrm{cpx}}\left(\text{Å}\right) = 1.066 - 0.104X_{\mathrm{Al}}^{\mathrm{M1,cpx}} - 0.212X_{\mathrm{Mg}}^{\mathrm{M2,cpx}} \quad , \quad (19)$$

$$E^{\mathrm{cpx}}\left(\mathrm{GPa}\right) = \left(2.27r_0^{\mathrm{cpx}} - 2.00\right)\times10^3 \quad , \quad (20)$$

where $X_{\mathrm{Al}}^{\mathrm{T,cpx}}$ is the Al content in the tetrahedral site of clinopyroxene (cpx) per formula unit; $X_{\mathrm{Al}}^{\mathrm{M1,cpx}}$ is the Al content in the M1 site; $X_{\mathrm{Mg}}^{\mathrm{M2,cpx}}$ is the Mg content in the M2 site assuming a random distribution of Fe-Mg in the M1 and M2 sites; $X_{\mathrm{H_2O}}^{\mathrm{melt}}$ is the molar fraction of H_2O in the melt; and T is temperature in Kelvin. Iron is assumed as Fe^{2+} for pyroxene formula calculations.

The lattice strain parameters for REE partitioning between plagioclase and melt take the following expressions (Sun et al., 2017):

$$\ln K_0^{\mathrm{plg}} = 16.05 - \frac{19.45 + 1.17P^2}{RT}\times10^4 - 5.17\left(X_{\mathrm{Ca}}^{\mathrm{plg}}\right)^2 \quad , \quad (21)$$

$$r_0^{\mathrm{plg}}\left(\text{Å}\right) = 1.179 \quad , \quad (22)$$

$$E^{\mathrm{plg}}\left(\mathrm{GPa}\right) = 196 \quad , \quad (23)$$

where $X_{\mathrm{Ca}}^{\mathrm{plg}}$ is the cation fraction of Ca in plagioclase (plg), and P is pressure in GPa. Uncertainties of the coefficients in equations (18–23) were not shown for simplicity but can be found in Sun and Liang (2012) and Sun et al. (2017). Although melt major element compositions appear to be unnecessary for the model calibration, they may indirectly affect REE partitioning through mineral-melt phase equilibria.

Together with these lattice strain parameters (equations (18–23)), equation (16) can then be used to quantify the effects of temperature, pressure, and composition on REE partitioning between plagioclase and clinopyroxene. The complete form of equation (16) can be rearranged to derive the REE thermometer for plagioclase-clinopyroxene systems:

$$B_i = T\left(\ln K_i^{\mathrm{plg/cpx}} - A\right) \quad , \quad (24)$$

$$A = 23.19 - 5.17\left(X_{\mathrm{Ca}}^{\mathrm{plg}}\right)^2 - 4.37X_{\mathrm{Al}}^{\mathrm{T,cpx}} - 1.98X_{\mathrm{Mg}}^{\mathrm{M2,cpx}} + 0.91X_{\mathrm{H_2O}}^{\mathrm{melt}}, \quad (25)$$

$$B_i = -32.04\times10^3 - 1.41\times10^3P^2 + 909.85G\left(r_i\right) \quad , \quad (26)$$

$$G\left(r_i\right) = -E^{\mathrm{plg}}\left(\frac{r_0^{\mathrm{plg}}}{2}\left(r_0^{\mathrm{plg}} - r_i\right)^2 - \frac{1}{3}\left(r_0^{\mathrm{plg}} - r_i\right)^3\right) + E^{\mathrm{cpx}}\left(\frac{r_0^{\mathrm{cpx}}}{2}\left(r_0^{\mathrm{cpx}} - r_i\right)^2 - \frac{1}{3}\left(r_0^{\mathrm{cpx}} - r_i\right)^3\right) \quad . \quad (27)$$

Note that G is the correction for changes in lattice strain energy and can be calculated using E and r_0 from equations (19–20) and (22–23). For anhydrous magmatic conditions or subsolidus mineral assemblages, $X_{H_2O}^{melt}$ in equation (25) should be neglected; for hydrous magmatic conditions, ±2 wt% of the melt water contents yield an uncertainty of about ±10 °C in the calculated temperatures (Sun & Liang, 2017). If the major and trace element compositions are provided for coexisting plagioclase and clinopyroxene, the temperature can be obtained through linear least-squares regression analyses of K_{REE} in the plot of (ln$K$–A) vs. B (Fig. 3) and is given by the slope of the straight line passing through the origin. For interested readers, Sun and Liang (2017) provided an Excel® spreadsheet to automate the temperature calculation using the REE-in-plagioclase-clinopyroxene thermometer.

Figure 5 shows an example of the temperature calculation for a gabbro sample (JC21-76R-6; Sun & Lissenberg, 2018a) from Hess Deep at the East Pacific Rise. In the spider diagram (Fig. 5a), heavy REE in plagioclase are close to or below detection limits because of their high incompatibility in plagioclase, and Eu is significantly apart from other REE due to its divalent behavior. Therefore, these elements should be excluded for accurate determination of the temperature. Through robust linear least-squares regression analyses, the remaining REE can define a straight line passing through the origin (Fig. 5b), the slop of which determines the temperature at 1118 ± 4 °C, similar to the crystallization temperatures of mid-ocean ridge basalts (e.g., Grove & Bryan, 1983). As an independent test, Sun and Liang (2017) also applied their REE thermometer to 12 volcanic rocks with coexisting plagioclase and clinopyroxene phenocrysts reported in the literature. They noted that temperatures of these samples derived from the REE thermometer are in good agreement with the plagioclase crystallization temperatures calculated using the plagioclase-melt thermometers (e.g., Putirka, 2005; Waters & Lange, 2015). This demonstrates that this REE thermometer can record crystallization temperatures of plagioclase in pre-eruptive magmatic conditions.

3.3.2. Mg-in-plagioclase-clinopyroxene thermometer

The Mg equilibrium exchange between plagioclase and clinopyroxene can be described through various chemical reactions, given the multiple endmembers in the two minerals and the multi-phase assemblages in natural petrological systems. The preferred reaction in Faak et al. (2013) is

$$[MgSiO_3]_{cpx} + [SiO_2] + [Al_2O_3] = [MgAl_2Si_2O_8]_{plg}\,, \quad (28)$$

where $MgSiO_3$ and $MgAl_2Si_2O_8$ are endmember components in clinopyroxene (cpx) and plagioclase (plg), respectively, and SiO_2 and Al_2O_3 may not be directly linked to any phases. In contrast, Sun and Lissenberg (2018a) suggested that the Mg exchange could be coupled together with Ca,

$$[Mg_2Si_2O_6]_{cpx} + [CaAl_2Si_2O_8]_{plg} = [CaMgSi_2O_6]_{cpx} + [MgAl_2Si_2O_8]_{plg}\,, \quad (29)$$

where $Mg_2Si_2O_6$ and $CaMgSi_2O_6$ can be replaced by other Mg- and Ca-endmember components in clinopyroxene (e.g., $MgAl_2SiO_6$ and $CaAl_2SiO_6$). Alternatively, the Mg exchange may also take place by reactions with other coexisting minerals (Sun & Lissenberg, 2018b):

$$[MgSiO_3]_{cpx} + 2[MgSiO_3]_{opx} + [Al_2O_3] = [Mg_2SiO_4]_{ol} + [MgAl_2Si_2O_8]_{plg}\,, \quad (30)$$

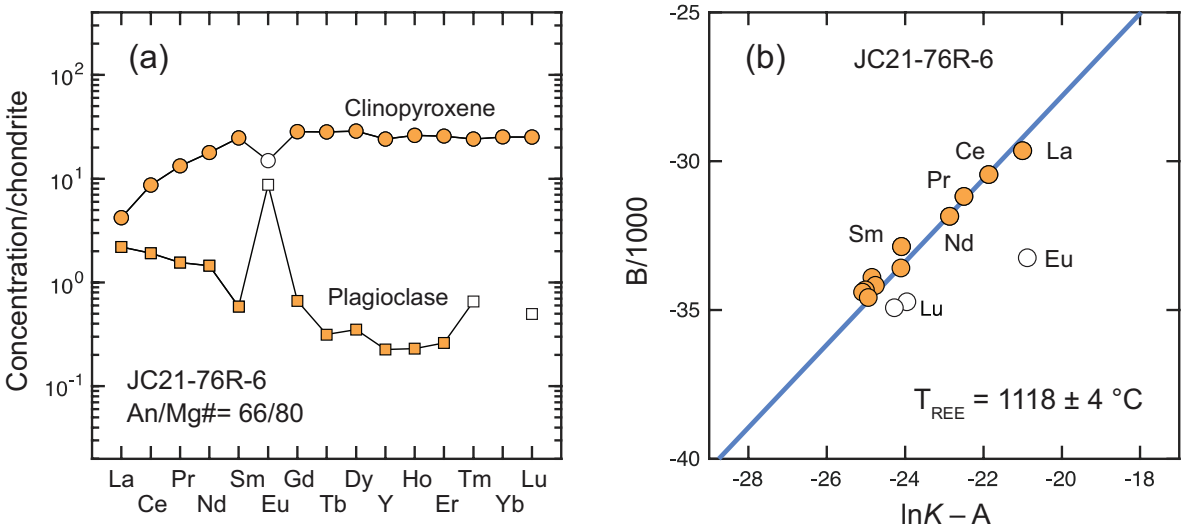

Figure 5. Temperature calculation using the REE-in-plagioclase-clinopyroxene thermometer for an oceanic gabbro (JC21-76R-6) from Hess Deep. Plot (**a**) shows the REE abundances in clinopyroxene and plagioclase normalized by chondrite compositions (Anders & Grevesse, 1989), and plot (**b**) displays the linear least-squares regression analysis of the REE partitioning data. The solid curve is the best-fit line passing through the origin. The temperature error was obtained from the regression analysis without considering the analytical uncertainties. In the temperature calculation, Eu was excluded for its divalent behavior, and heavy REE in plagioclase were also excluded because of their large analytical uncertainties.

where opx and ol denote orthopyroxene and olivine, respectively.

Given these multiple choices of Mg exchange between plagioclase and clinopyroxene, chemical reactions need to be carefully selected to reduce the complexities for thermometer calibration and application. Thermometers derived from equation (28) require independent constraints on SiO_2 and Al_2O_3 activities, while those calibrated using equation (30) are only applicable to rocks with four coexisting minerals (i.e., ol, opx, cpx, and plg) and known Al_2O_3 activities. With the aforementioned limitations, these types of exchange reactions are not practical for thermometer applications to natural samples. On the other hand, equation (29) appears to be more promising as it postulates minimum assumptions regarding the coexisting mineral assemblages and the knowledge of SiO_2 and/or Al_2O_3 activities. Although additional minerals and activities of SiO_2 or Al_2O_3 are not included in equation (29), they may still indirectly influence the Mg–Ca coupled exchange through the compositions of major elements in plagioclase and clinopyroxene. For instance, changing the SiO_2 activity can potentially modify the anorthite component in plagioclase ($CaAl_2Si_2O_8$) and the Ca-Tschermak component in clinopyroxene ($CaAl_2SiO_6$) and, in turn, affect Mg partitioning through the Mg–Ca coupled exchange reaction (equation (29)).

Many phase equilibria experiments in the literature have produced plagioclase and clinopyroxene coexisting with silicate melts (e.g., Grove & Bryan, 1983; Sack et al., 1987; Sisson & Grove, 1993; H.-J. Yang et al., 1996; Thy et al., 1998; Grove et al., 2003; Villiger et al., 2004; Takagi et al., 2005; Feig et al., 2006). Unfortunately, because the qualities of Mg data in plagioclase are highly variable, the existing phase equilibria experiments cannot be used directly for the Mg thermometer calibration. Similar to the multi-element approach for thermometer calibration (Section 3.2), Sun and Lissenberg (2018a) calculated plagioclase-clinopyroxene K_{Mg} for existing phase equilibria experiments by combining the previously calibrated plagioclase-melt K_{Mg} model (Sun et al., 2017) with the measured clinopyroxene-melt K_{Mg} from the phase equilibria experiments. These phase-equilibria experiments cover a wide range of temperatures (800–1430 °C), pressures (0.0001–2.7 GPa) and compositions (e.g., An# = 28–100 in plagioclase). Through multiple linear least-squares regression analyses of the plagioclase-clinopyroxene K_{Mg} data, Sun and Lissenberg (2018a) calibrated a new thermometer using the Mg–Ca coupled exchange (equation (29)):

$$T(K) = \frac{14265 + 487P^2}{5.15 - \ln\left(C_{MgO}^{plg} / C_{MgO}^{cpx}\right) + 0.75\left(X_{An}\right)^2}, \quad (31)$$

where C_{MgO} is the weight fraction of MgO in plagioclase (plg) or clinopyroxene (cpx), and X_{An} is the molar fraction of anorthite in plagioclase [X_{An} = Ca/(Ca+Na+K) in mole]. Uncertainties of the coefficients in equation (31) can be found in Sun and Lissenberg (2018a). The regression analyses yield a standard error of ±29 °C for this thermometer. As demonstrated in Sun and Lissenberg (2018a), the plagioclase-clinopyroxene K_{Mg} data from the diffusion experiments of Faak et al. (2013) further validate the accuracy of this Mg-

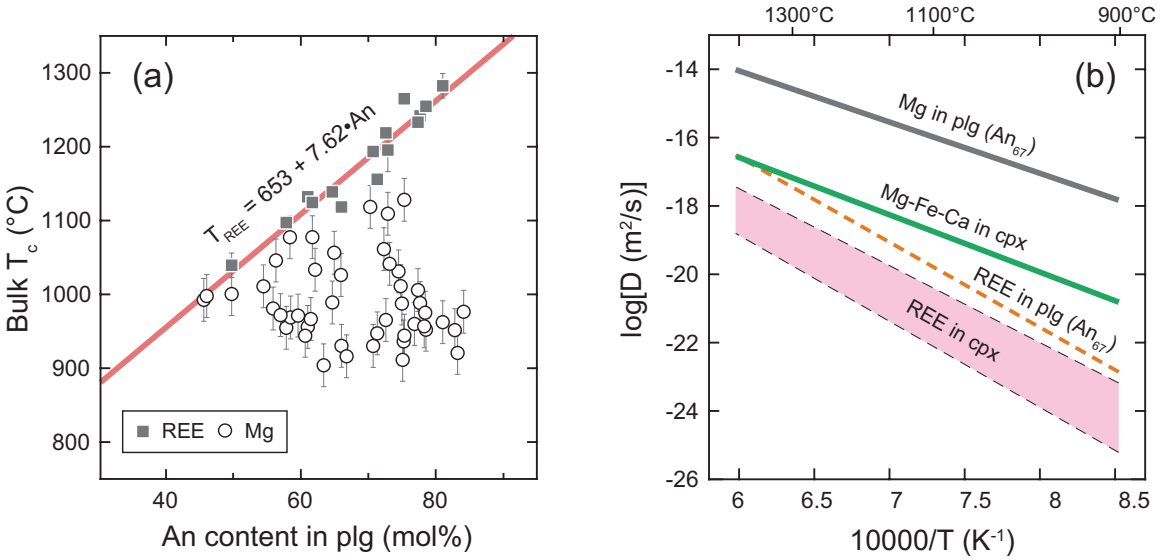

Figure 6. Plots showing (**a**) the thermometer-derived Mg and REE bulk closure temperatures of Hess Deep samples and (**b**) the experimentally-determined diffusion coefficients of Mg and REE in plagioclase and in clinopyroxene. Solid line in (**a**) displays the strong positive correlation between REE closure temperatures and plagioclase anorthite contents (Sun & Lissenberg, 2018a). Errors of Mg closure temperatures were taken from the Mg-exchange thermometer calibration (±29 °C). The diffusion coefficients of REE in clinopyroxene were calculated at 2 kbar using the diffusion parameters from Van Orman et al. (2001), while those of REE in plagioclase (X_{An} = 0.67) were calculated using the diffusion parameters of Nd from Cherniak (2003). Mg diffusion coefficients in plagioclase were taken from Van Orman et al. (2014), and those in clinopyroxene were taken from Müller et al. (2013).

based thermometer.

Applications of the Mg- and REE-based geothermometers to oceanic gabbros from Hess Deep indicate systematical differences in temperatures recorded by Mg and REE (Fig. 6a). The calculated REE temperatures (T_{REE} = 1040–1283 °C) are similar to the crystallization temperatures of mid-ocean ridge basalts (e.g., Grove & Bryan, 1983) and are also positively correlated with the anorthite contents in plagioclase (An#) that have been widely used as a qualitative index to track magma crystallization. However, the calculated Mg temperatures (T_{Mg} = 904–1128 °C) are generally about 39–320 °C lower than T_{REE} and do not correlate with An#, indicating extensively diffusive resetting of Mg at lower temperatures after the main stages of crystallization. Given that the two different thermometers were applied to the same cumulate rocks, the most possible causes for the systematic differences between T_{Mg} and T_{REE} are the differential diffusive responses of Mg and REE to changes in temperature after crystallization of the cumulus minerals. As shown in Fig. 6b, the diffusion coefficients of Mg in plagioclase are about 2–4 orders of magnitude greater than those of REE in plagioclase, supporting the faster diffusive resetting of Mg in the plagioclase-clinopyroxene system. Thus, for mafic cumulate rocks, the REE-based exchange thermometer can potentially record temperatures at or close to the crystallization of cumulate minerals, whereas the Mg-based exchange thermometer is likely more sensitive to diffusive re-distribution during cooling.

4. Trace element-based geospeedometry

Extraction of thermal histories from rock records by geospeedometers relies on the quantitative measurement of mineral diffusive responses to changes in temperature. Without significant crystal overgrowth after the main stages of crystallization, such diffusive response manifests in the compositional variation. Major controls of the compositional variation include the rate of temperature changes, the initial conditions of temperature and concentration, and the diffusion coefficient of the element of interest in the mineral, as well as a number of other factors, such as the partition coefficient of the element between the mineral and surroundings, the size of the mineral grain, and the relative phase proportions of the mineral assemblage (e.g., Dodson, 1973, 1986; Lasaga et al., 1977; Lasaga, 1983; Eiler et al., 1992; Ehlers & Powell, 1994; Ganguly & Tirone, 1999; Yao & Liang, 2015; Liang, 2015; Watson & Cherniak, 2015; Sun & Lissenberg, 2018a). Thus, the design and application of geospeedometers are not as straightforward as those of geothermometers. In this section, I first provide a general overview of diffusion and geospeedometry in petrological systems, then outline the basic idea of geospeedometer design, and lastly present the recent progress in geospeedometry for mafic cumulate rocks.

4.1. Diffusion and geospeedometry

4.1.1. A brief overview

According to the phenomenological analysis of Darken (1948), the diffusive flux (J) of a trace element of interest can be described as

$$J = -D^* \frac{\partial C}{\partial x} = -D\left(1+\frac{\partial \ln \gamma}{\partial \ln C}\right)\frac{\partial C}{\partial x} \ , \tag{32}$$

where x is the spatial coordination. The intrinsic diffusivity (D) can be determined in diffusion experiments through the Arrhenius equation:

$$D = D_0 \exp\left(-\frac{E_A}{RT}\right) , \tag{33}$$

where E_A is the activation energy, and D_0 is the pre-exponential factor indicating the maximum diffusion coefficient at infinite temperature. When the activity coefficient (γ) of a trace element is independent of its concentration (C), its diffusive flux reduces to

$$J = -D\frac{\partial C}{\partial x} \ . \tag{34}$$

However, when γ varies with the concentration of a major element (X), the diffusive flux of this trace element takes the following expression:

$$J = -D\left(\frac{\partial C}{\partial x}+\frac{\partial \ln \gamma}{\partial x}C\right) = -D\left(\frac{\partial C}{\partial x}+\frac{\partial \ln \gamma}{\partial X}\frac{\partial X}{\partial x}C\right) . \tag{35}$$

As shown in equation (35), the major element, if manifesting zonation ($\partial X/\partial x \neq 0$), can enhance or reduce the diffusive flux of the trace element, depending on the sign of $\partial \ln\gamma/\partial X$ and the major element zoning pattern ($\partial X/\partial x$) (Sun & Lissenberg, 2018b). Additional influence of the major element may arise from D when it is dependent on X.

Assuming chemical diffusion is the only mass transport process in the system (e.g., no radiogenic decay/ingrowth, or extensive crystal overgrowth), the concentration of a given chemical species varies with time (t) and the net diffusive flux and can be described through the continuity equation:

$$\frac{\partial C}{\partial t} + \nabla \bullet J = 0 \ . \tag{36}$$

By substituting equation (35) into equation (36), a general expression can be obtained to describe the isotropic diffusion of a trace element in a crystal:

$$\frac{\partial C}{\partial t} = \frac{1}{r^{n-1}}\frac{\partial}{\partial r}\left[r^{n-1}D\left(\frac{\partial C}{\partial r}+\frac{\partial \ln \gamma}{\partial X}\frac{\partial X}{\partial r}C\right)\right] , \tag{37}$$

where r is the spatial coordinate from the center of the crystal, and n indicates the geometries (1 – plane sheet, 2 – cylinder, and 3 – sphere) approximating crystal shapes in one-, two-, and three-dimensional spaces. Assuming negligible effects of major elements on γ, equation (37) can be simplified to the familiar diffusion equation:

$$\frac{\partial C}{\partial t}=\frac{1}{r^{n-1}}\frac{\partial}{\partial r}\left[r^{n-1}D\frac{\partial C}{\partial r}\right] . \quad (38)$$

Assuming that the cooling system starts from chemical equilibrium, the initial (C_0) and boundary concentrations (C_b) are determined by the partition coefficient (K) between this crystal (α) and its surrounding phase (β):

$$C_0^{\alpha}=K\left(T_0\right)\cdot C_0^{\beta} , \quad (39)$$

$$C_b^{\alpha}=K\left(T\right)\cdot C_b^{\beta} , \quad (40)$$

where $K(T_0)$ and $K(T)$ denote partition coefficients at the initial (T_0) and instantaneous temperatures (T), respectively. The temperature dependence of partition coefficients can be experimentally calibrated using equation (7) or (16). If the system is approximately closed, an additional boundary constraint comes from the balance of total diffusive flux between this crystal and its surrounding phase:

$$\phi^{\alpha}\frac{D^{\alpha}}{L^{\alpha}}\frac{\partial C^{\alpha}}{\partial r}\bigg|_{r=L^{\alpha}}=\phi^{\beta}\frac{D^{\beta}}{L^{\beta}}\frac{\partial C^{\beta}}{\partial r}\bigg|_{r=L^{\beta}} , \quad (41)$$

where ϕ denotes the modal abundance, and L is the effective grain radius. However, this boundary constraint becomes unnecessary when the surrounding phase has no compositional responses to diffusion in the crystal, i.e., phase β has a constant and homogeneous concentration profile. In this case, the surrounding phase behaves as a homogeneous infinite reservoir, and accordingly the initial and boundary conditions defined in equations (39) and (40) are sufficient to solve diffusion in the single crystal.

In a cooling petrological system (Fig. 7), the crystal boundary has instant responses to temperature changes and thus causes a concentration gradient driving diffusion between the interior and boundary. If chemical disequilibrium is imposed initially as zonation in the crystal (e.g., stepwise profiles) due to different stage of formation, diffusion could commence immediately within the crystal. Because D decreases exponentially with temperature (equation (33)), chemical diffusion effectively reaches closure at a lower temperature, leaving a stabilized concentration profile, i.e., the closure profile (Dodson, 1986) in the crystal (Fig. 7). The corresponding temperature is called the closure temperature (Dodson, 1973). Applying the relevant geothermometers to the mean or local concentration of the closure profile, one could obtain two types of closure temperatures, i.e., the bulk and local closure temperatures (Dodson, 1973, 1986). Accordingly, cooling rates can be estimated using the local closure profile (or local closure temperature), i.e., the grain-scale diffusion approach, or using the mean concentration of the crystal (or bulk closure temperature), i.e., the bulk diffusion approach. Through analytical and numerical analyses of equation (38) or its approximate forms, both approaches have been widely used to model cooling histories of various petrological systems (e.g., Dodson, 1973, 1986; Lasaga et al., 1977; Lasaga, 1983; Eiler et al., 1992; Ehlers & Powell, 1994; Ganguly & Tirone, 1999; Yao & Liang, 2015; Liang, 2015; Watson & Cherniak, 2015; Sun & Lissenberg, 2018a).

4.1.2. Single crystals within infinite reservoirs

A simple scenario formulated in the seminal works of Dodson (1973, 1986) is a single crystal within an infinite reservoir, in which the relative proportions of individual minerals can be omitted. To linearize this diffusion problem, Dodson (1973, 1986) assumed that both the reciprocal temperature ($1/T$) and boundary concentration (C_b) vary uniformly with time (t):

$$\frac{E_A}{RT}=\frac{E_A}{RT_0}+t/\tau , \quad (42)$$

$$C_b=C_0+bt/\tau , \quad (43)$$

where τ is the characteristic time constant for an e-folding decrease of diffusivity (cf. equation (33)) during cooling, and b is a constant of temporary use. The cooling time constant (τ) is related to the absolute cooling rate (dT/dt) at an instantaneous temperature (T) following the expression:

$$\tau=-\frac{RT^2}{E_A\left(dT/dt\right)} . \quad (44)$$

Through an analytical approach, Dodson (1973, 1986) derived a simple expression relating the closure temperature (T_c) to the instantaneous cooling rate (dT/dt) at T_c:

$$T_c=\frac{E_A/R}{\ln\left[-\tau D_0/L^2\right]+\Gamma}=\frac{E_A/R}{\ln\left[\frac{RT_c^2D_0}{E_A\left(dT/dt\right)L^2}\right]+\Gamma} , \quad (45)$$

where Γ is the closure function depending upon crystal geometry and location in the crystal. Interested readers are referred to Table 2 in Dodson (1986) for the spatially variable Γ that enables the calculation of a local closure temperature profile using equation (45). The spatially weighted average of Γ is 4.0066 for sphere, 3.29506 for cylinder, and 2.15821 for plane sheet, which give rise to the bulk closure temperatures for corresponding geometries.

According to Dodson's formulation (equation (45)), the closure temperature for diffusion in a single crystal is positively correlated with the cooling rate and grain size but increases with the decrease of diffusivity (Mg vs. REE; Fig. 8a). The cooling rate (dT/dt) and the square of grain radius (L^2) can be conveniently treated together by their product as a single term bearing the meaning of cooling rates, i.e., the *effective cooling rate*. As shown in Fig. 8b, the bulk closure temperature derived from Dodson's formulation for a given element always follows a single curve as a function of the effective cooling rate, regardless of the initial conditions. This effect is due to the simplification adopted by Dodson (1973, 1986) that only takes account of cases with extensive diffusion and complete loss of the initial conditions (i.e., T_0 and C_0) in

the crystal. If the assumptions of Dodson (1973, 1986) regarding the extensive diffusion and infinite reservoir can be justified for natural single-crystal systems, equation (45) could then be applied to estimate the rate of cooling using either the bulk closure temperature or the closure (temperature) profile of the crystal.

To incorporate arbitrary small amount of diffusion in Dodson's formulation, Ganguly and Tirone (1999) introduced a numerical correction term for the closure function (Γ) in equation (45), which depends on the initial temperature and crystal geometry. Closure temperatures from the two formulations are consistent for systems with slow cooling rates and/or small grain radii. However, for systems with rapid cooling rates and/or large grain sizes, closure temperatures derived from the formulation of Ganguly and Tirone (1999) remain close to the corresponding initial temperatures (Fig. 8b), indicating the necessity of correction for the closure function. Notably, the closure temperatures of slower diffusing species (e.g., REE) are more resistant to diffusive resetting of the initial condition than those of faster diffusing species (e.g., Mg). Given the potential effect of initial conditions on closure temperatures, estimation of cooling rates using the formulation of Ganguly and Tirone (1999) for natural single-crystal systems thus demands a prior assumption or an independent determination of the equilibrium initial conditions. In particular, for single-crystal systems with stepwise initial concentration profiles, Watson and Cherniak (2015) developed a parameterized expression from their numerical solutions to constrain the cooling history.

4.1.3. Two- or multi-mineral assemblages

For cooling petrological systems with two or more minerals, simple analytical expressions have not been obtained following the approach of Dodson (1973, 1986). Using a second-order polynomial approximation for the diffusion profile of each crystal in the bi-mineral system, Liang (2015) simplified the familiar diffusion equation (equation (38); i.e., first-order derivative in time and second-order in space) to first-order transport equation (i.e., first-order derivatives in both time and space). Assuming that the system

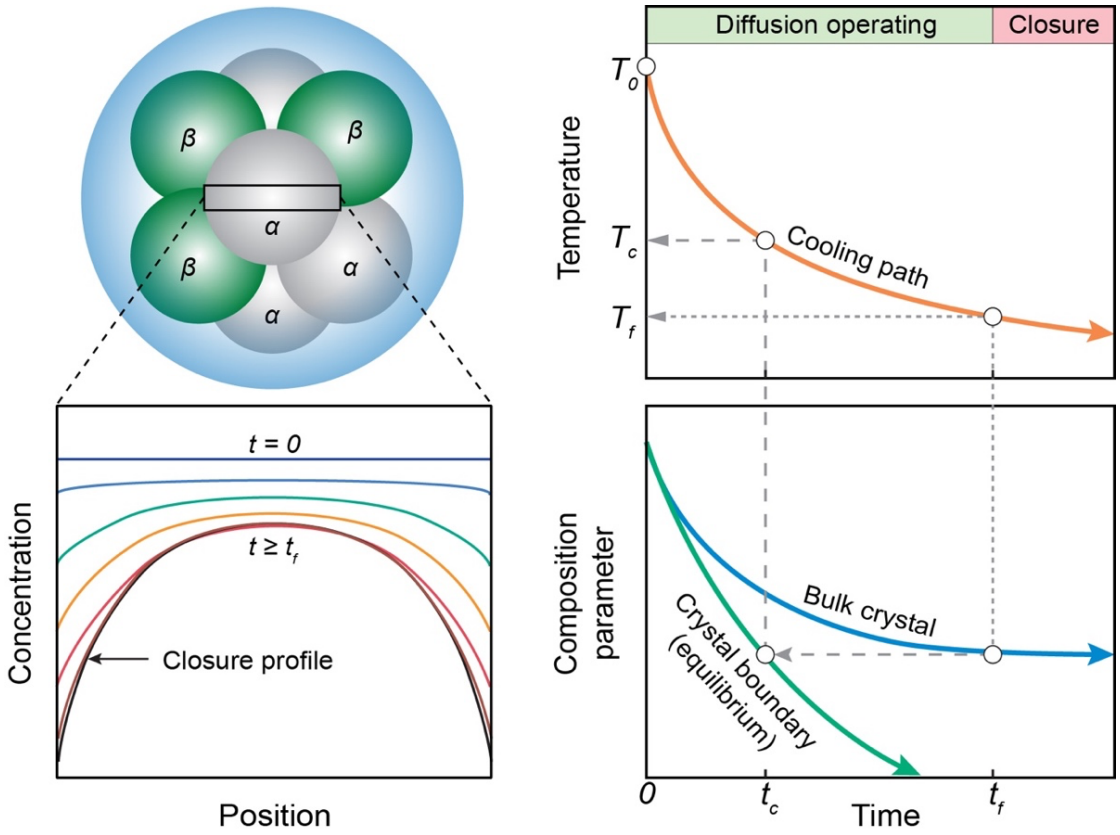

Figure 7. Schematic diagrams showing the closure profile and temperature of a cooling petrological system. During cooling, the crystal surface remains in chemical equilibrium with the surroundings, which generates a concentration gradient from the interior to drive diffusion. Due to diffusive interaction with the surroundings, the initial concentration profile of the crystal becomes progressively concave through time (t) but will be effectively locked at a certain point ($t = t_f$), marking the closure of diffusion in the crystal. The locked concentration profile is called the closure profile (Dodson, 1986). Similarly, the chemical composition of the crystal or other equivalent parameters (e.g., concentration ratios with the surroundings) would also become asymptotically invariant after a certain time. The invariant value is directly measurable from natural petrological systems at diffusive closure ($t \geq t_f$) and can then be related to an equilibrium temperature at an earlier time ($t = t_c$). This "equilibrium" temperature, named as the closure temperature (T_c) by Dodson (1973), is apparently lower than the initial temperature (T_0) and greater than the ambient temperature (T_f) at the time of diffusive closure ($t = t_f$).

has not been open to mass transfer with their surrounding media during cooling, Liang (2015) constructed an analytical expression to describe the bulk closure temperature of a trace element in cooling bi-mineral systems:

$$\frac{\phi_\beta E_{A,\alpha} L_\alpha^2 \left(dT/dt\right)_{T_c} / D_{\alpha,T_c} + \phi_\alpha E_{A,\beta} L_\beta^2 \left(dT/dt\right)_{T_c} K_{T_c} / D_{\beta,T_c}}{\left(\phi_\alpha K_{T_c} + \phi_\beta\right) RT_c^2} + \frac{\phi_\beta \phi_\alpha K_{T_c} E_K}{\left(\phi_\alpha K_{T_c} + \phi_\beta\right)^2 RT_c^2} \left(\frac{L_\alpha^2}{D_{\alpha,T_c}} - \frac{L_\beta^2}{D_{\beta,T_c}}\right) \left(dT/dt\right)_{T_c} = \exp\left(\Gamma\right) , \quad (46)$$

where quantities with subscript T_c indicate that they are evaluated at T_c, Γ is the spatially averaged closure function from the formulation of Dodson (1973, 1986) (equation (45)), and E_K is the activation energy of partitioning (= B•R; B is defined in equation (10)). Because the corrected closure function (Γ) of Ganguly and Tirone (1999) for diffusion in single crystals is not applicable to bi-mineral systems, arbitrary small amount of diffusion was not taken into account in equation (46) to incorporate the effects of large grain sizes and initial temperatures. Thus, direct estimation of cooling rates using equation (46) can only be made for bi-mineral systems with complete loss of the initial conditions.

This analytical expression (equation (46)) of Liang (2015) enables the scale analysis on the relative importance of individual minerals for determining the bulk closure temperature of a trace element in the cooling bi-mineral system. Introducing two short-hand notations (Θ and ω), Sun and Liang (2017) rewrote equation (46) as a Dodson-type expression:

$$T_c = \frac{E_{A,\alpha}/R}{\ln\left[\frac{RT_c^2 D_{0,\alpha}}{E_{A,\alpha}\left(dT/dt\right)L_\alpha^2}\right] + \Gamma + \ln\left(\Theta\right)} , \quad (47)$$

$$\Theta = \frac{1 + \left(\phi_\alpha/\phi_\beta\right)K_{T_c}}{1 + \left(\phi_\alpha/\phi_\beta\right)\omega K_{T_c}} , \quad (48)$$

$$\omega = \frac{D_{\alpha,T_c}}{D_{\beta,T_c}} \frac{L_\beta^2}{L_\alpha^2} \left(\frac{E_{A,\beta} + E_K}{E_{A,\alpha}}\right) - \frac{E_K}{E_{A,\alpha}} , \quad (49)$$

where Θ is a correction factor for the effects of diffusion, partitioning, and relative proportions of the coexisting minerals (α and β), and ω denotes the relative diffusion rates in the two minerals. It is important to note that due to various effects from the surrounding phase, the closure temperature of a bi-mineral system cannot be simply taken as that of a single crystal. As shown in equation (48), the relative diffusion rate (ω) is the primary factor controlling the bulk effect (Θ) of the surrounding phase. When the two minerals have comparable diffusion rates (ω = 1), the bulk effect of the surrounding phase becomes negligible (Θ = 1 → ln(Θ) = 0), which reduces equation (47) to the formulation (equation (45)) of Dodson (1973, 1986). In this case, the surround phase β effectively becomes an infinite reservoir for diffusion in mineral α, and thus the closure temperature formulations for single-crystal systems (e.g., equation (45)) likely remain valid. However, when the relative diffusion rates in the two minerals are distinct from each other ($|\omega - 1| >> 0$), the bulk effect of the surrounding phase (Θ) can exert sufficient influences ($|\ln(\Theta)| >> 0$) to make the bi-mineral closure temperature

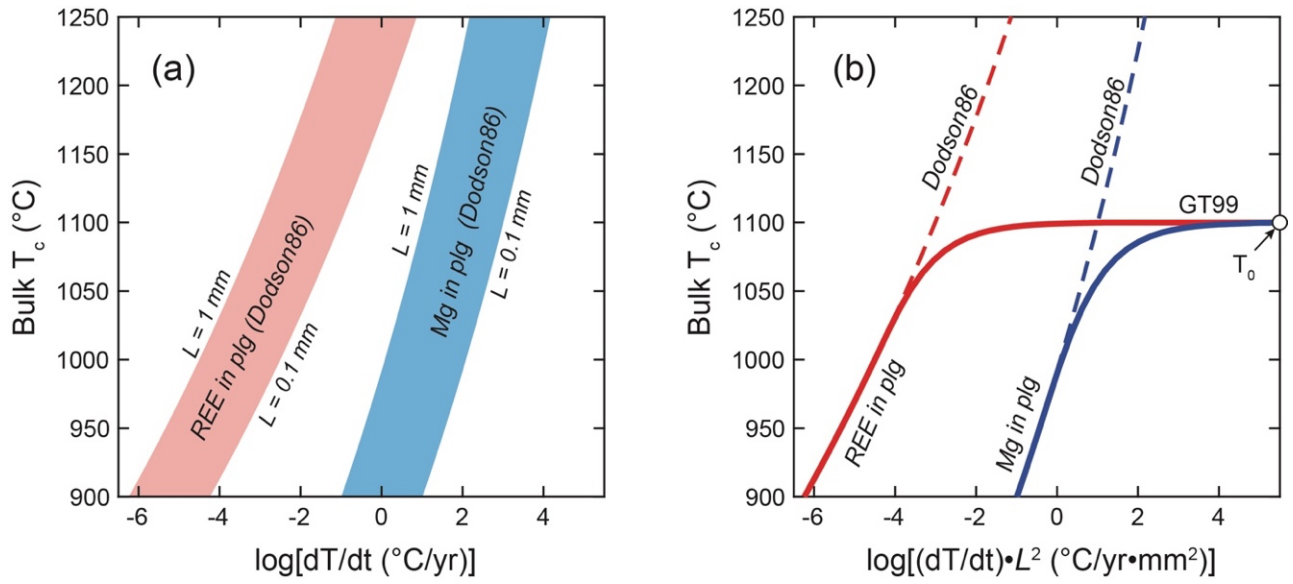

Figure 8. Comparison of bulk closure temperatures derived from the formulations of Dodson (1986) and Ganguly and Tirone (1999; GT99) for REE and Mg in spherical plagioclase crystals within a homogeneous infinite reservoir. The cooling rates in (**a**) are absolute cooling rates, while those in (**b**) are the effective cooling rates, i.e., the products of grain radius squares (L^2) and cooling rates (dT/dt). Two different grain radii (0.1 and 1 mm) were used in the closure temperature calculations. See Fig. 6 for the references of Mg and REE diffusion data.

significantly derivate from that of the single crystal. Under this condition, a numerical analysis of equation (38), as shown in previous studies (e.g., Lasaga et al., 1977; Eiler et al., 1992; Ehlers & Powell, 1994; Yao & Liang, 2015; Sun & Lissenberg, 2018a), is necessary for a more comprehensive understanding on the cooling histories.

4.2. Basic idea of geospeedometer design

The goal of geospeedometry is to conveniently extract the cooling history information from the diffusive relaxation of petrological systems that can be measured through closure temperatures (i.e., equivalent to closure profiles). As discussed in Section 4.1, the closure temperature (T_c) of the system can be described in general as

$$T_c = f\left(T_0, dT/dt, \Omega\right) , \tag{50a}$$

$$\Omega = \left\{D, K, \phi, L\right\} , \tag{50b}$$

where f denotes an unspecified expression defined by the analytical or numerical solution of the diffusion equation, and Ω is a set of directly measurable variables including the diffusion coefficients (D), phase proportions (ϕ), grain radii (L), and partition coefficient(s) (K) of the mineral(s) in the petrological system. If the system starts cooling from disequilibrium concentration profiles, the initial concentration (C_0) should also be considered as an additional variable. In addition to the cooling rate (dT/dt), the initial condition (i.e., T_0 and C_0) can significantly influence the closure temperatures (or profiles) for systems with relatively rapid cooling rates and/or large grain radii. As shown in Fig. 8b for a single crystal in a homogeneous infinite reservoir, without knowing the relevant T_0, it is easy to mistakenly underestimate the cooling rate by several orders of magnitude using the observed closure temperatures. Moreover, as the initial point of the cooling path (Fig. 7), T_0 is also important for estimation of the cooling time scale for the petrological system.

Because cumulate rocks have simple monotonic cooling paths after the main stages of crystallization, T_0 of cumulate rocks are effectively the mean temperatures of cumulus crystallization and hence are of significant importance for understanding magmatic histories of cumulate parental melts. Estimation of T_0 for cumulate rocks depends not only on the precision of geothermometers but also on the extent of diffusive resetting (i.e., equivalent to closure temperatures) of key elements used in the geothermometers. In general, slowly diffusing elements tend to have small extents of diffusive relaxation and thus likely record closure temperatures close to conditions of mineral crystallization (e.g., Wark & Watson, 2006; Watson et al., 2006; Liang et al., 2013; Sun & Liang, 2015, 2017). However, at smaller effective cooling rates ($L^2 \bullet dT/dt$; Section 4.1.2), elements with slow diffusivities (e.g., REE) could also be extensively reset to lower temperatures (Fig. 8). Given the codependent relation between closure temperatures and cooling histories (i.e., T_0 and dT/dt; equation (50a)), it is challenging to determine the full cooling path

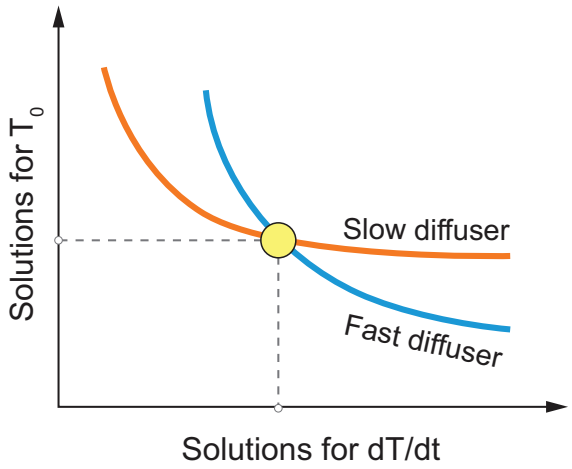

Figure 9. Schematic illustration showing the determination of initial temperature (T_0) and cooling rate (dT/dt) for a cooling petrological system. As T_0 and dT/dt both affect the measured closure temperatures, one may find a family of possible solutions for T_0 and dT/dt using the closure temperatures of single elements. The combination of two elements with distinct partitioning and diffusion behaviors could simultaneously constrain the two unknowns (T_0 and dT/dt) from the intercept of two series of solutions.

(including both T_0 and dT/dt) from the measured closure temperatures (or profiles) of single elements.

A promising resolution to this problem is the combination of two or multiple elements with distinct geochemical behaviors in diffusion and/or partitioning. Following equation (50a), the closure temperatures of two elements (i vs. j) can be written as:

$$T_c^i = f\left(T_0, dT/dt, \Omega_i\right) , \tag{51a}$$

$$T_c^j = g\left(T_0, dT/dt, \Omega_j\right) . \tag{51b}$$

Given their distinct geochemical behaviors, the two elements have unique Ω and explicit expressions (f vs. g) of closure temperatures. From the measured closure temperatures of each element, one may obtain a family of solutions for T_0 and dT/dt; however, when considered together, the two families of solutions may intercept at a singular point that determines both T_0 and dT/dt for the petrological system (Fig. 9). This approach has been detailed recently in the framework of differential responses of bulk closure temperatures by Sun and Lissenberg (2018a), while similar ideas were also suggested in several previous studies (e.g., Watson & Harrison, 1984; Costa & Dungan, 2005; Morgan & Blake, 2006; Watson & Cherniak, 2015; Sun & Liang, 2017).

4.3. The Mg–REE coupled geospeedometer for mafic cumulates

For mafic cumulate rocks, two different geothermometers have been calibrated based on the partitioning of REE and Mg, respectively, between plagioclase and clinopyroxene (see

Section 3.3). As shown in Fig. 6a, the closure temperatures of REE and Mg derived from the two thermometers appear to be systematically distinct from each other for oceanic gabbros, which can be explained by the relative differences in their diffusivities (Fig. 6b). Following the idea outlined in Section 4.2, the differential diffusive closures of Mg and REE in plagioclase-clinopyroxene systems are suitable for constructing a generalized geospeedometer to determine the full cooling path of mafic cumulate rocks (Sun & Lissenberg, 2018a). In addition to the two geothermometers, however, implementation of this idea also requires establishing the exact expressions of the closure temperatures (equation (50a)) from analytical or numerical solutions of the diffusion equation.

4.3.1. Diffusion model

Mafic cumulate rocks with plagioclase and clinopyroxene as the major cumulus phases can be effectively treated as two-mineral aggregates for diffusion modeling. Given their significantly different diffusivities (Fig. 6b), plagioclase and clinopyroxene in this two-mineral system has distinct diffusion rates of Mg or REE ($\omega >> 1 \rightarrow \ln(\Theta) << 0$; see equation (47)) and thus cannot be considered simply as a single crystal in an infinite reservoir that has been formulated previously with analytical solutions (e.g., Dodson, 1973, 1986; Ganguly & Tirone, 1999). Accordingly, numerical models are required to build the explicit expressions for Mg and REE closure temperatures in this two-mineral system. As both minerals are important for determining the measured closure temperatures or profiles, the grain-scale diffusion approach has to consider the closure profiles of individual crystals in the plagioclase-clinopyroxene aggregate to obtain the representative cooling information. Because cross-section analysis of trace elements requires more dedicated protocols and analytical facilities, often one or two selected profiles are measured for grain-scale diffusion modeling, which apparently introduces a significant bias for this two-mineral diffusion system. Instead, the bulk diffusion approach is more practical, because the averaged mineral compositions can be routinely measured through in situ analyses of cores and rims in multiple representative grains of each mineral.

Numerical modeling of trace element diffusion commonly solves the familiar diffusion equation (equation (38)) through finite difference methods. For bulk diffusion simulations of a trace element (i.e., Mg and REE), the plagioclase-clinopyroxene system can be approximated as an aggregate of two types of spherical mineral grains, and chemical diffusion has to be solved simultaneously in both plagioclase and clinopyroxene along a prescribed cooling path. Similar to Dodson (1973, 1986), the monotonic cooling profile of cumulate rocks can be described as a reciprocal function of time in the diffusion simulations:

$$1/T = 1/T_0 + \eta \bullet t \ , \tag{52a}$$

$$\eta = \left(dT/dt\right)_{T_0} \Big/ \left(T_0\right)^2 = \left(dT/dt\right)_{T_c} \Big/ \left(T_c\right)^2 \ , \tag{52b}$$

where η is a cooling constant determined by the absolute initial cooling rate. As shown in equation (52b), the (absolute) cooling rates decrease at lower temperatures and can be adjusted for instantaneous temperatures. The initial and boundary conditions of the two types of minerals are constrained by equation (39–41), the temperature-dependent partition coefficients (K_{REE}: equations (24–27); K_{Mg}: equation (31)), and the temperature-dependent diffusion coefficients in plagioclase (equations (A14 and A15) in Sun & Lissenberg, 2018a) and in clinopyroxene (Van Orman et al., 2001; Müller et al., 2013). Note that equations (A14) and (A15) in Sun and Lissenberg (2018a) are parameterized Arrhenius equations using the Mg diffusion data of Faak et al. (2013) and Van Orman et al. (2014) and the REE diffusion data of Cherniak (2003), respectively. The closure of diffusive exchange, following Dodson (1973, 1986), can be defined by the asymptote of apparent bulk partition coefficients. Interested readers are referred to Appendix A in Sun and Lissenberg (2018a) for details of the numerical methods and calculations of bulk closure temperatures.

It has been suggested that the anorthite zonation in plagioclase can influence the diffusive relaxation of Mg in plagioclase (e.g., Costa et al., 2003). According to equation (35), additional diffusive fluxes may come from the major element dependent activity coefficients. Although rigorous activity models have not been constructed for trace elements in minerals, they could be inferred from the partitioning model or its equivalents (e.g., exchange geothermometers) according to the scaling relation between the activity coefficient and relevant major elements. Incorporating the effect of anorthite zoning, Sun and Liang (2017) solved the more complete form of diffusion equation (equation (37)) for Mg and REE diffusion in two representative aggregates with normally zoned plagioclase. However, their simulation results indicate negligible influences on the calculated bulk closure temperatures. Given that natural cumulate rocks likely have various types of zoning patterns in plagioclase, the integrated effects of anorthite zoning, if any, are anticipated to be insignificant for the bulk diffusion in the two-mineral aggregate.

4.3.2. Determination of the cooling path

Figure 10 shows an example of the numerical calculations for Mg and REE diffusion in a cooling plagioclase-clinopyroxene aggregate with a uniform grain radius and equal mineral mode. The imposed cooling paths were defined by four equilibrium initial temperatures (1000–1300 °C) and a wide range of effective cooling rates (10^{-7}–10^{3} °C/yr·mm^2). The calculated bulk closure temperatures of REE (T_{REE}; solid curves) and Mg (T_{Mg}; dashed curves) define two regimes, a slow- and a fast-cooling regime (Fig. 10a). The boundaries of these two regimes are controlled by the "Dodson limit" corresponding to bulk closure temperatures for a "sufficiently high initial temperature" but importantly varying as a function of Ω (see equation (50a); Sun & Lissenberg, 2018a). Within the two regimes, the differential responses of T_{REE} and T_{Mg} to

the same cooling path enable one to establish their explicit expressions (equation (50a)) and further to uniquely constrain both T_0 and dT/dt of the cooling path. However, for extremely slow cooling, both T_{REE} and T_{Mg} may lose the memory of initial conditions and fall on their Dodson limits; for very rapid cooling, both T_{REE} and T_{Mg} likely remain at T_0 and thus are unable to determine dT/dt.

The simultaneous inversion of T_0 and dT/dt could be visualized by plotting the differences between T_{REE} and T_{Mg} as a function of T_{REE} (Fig. 10b). The maximum differences between T_{REE} and T_{Mg} define the upper boundary in Fig. 10b and are equivalent to the Dodson limit of REE. The background curves in Fig. 10b are two families of contours for the numerically calculated bulk closure temperatures: the dashed curves are isopleths of dT/dt, while the solid curves are isopleths of T_0. The two families of isopleths intercept at singular points that uniquely define T_0 and dT/dt. For instance, T_{REE} (1080 °C) and T_{Mg} (800 °C) of a hypothetical sample place it at the intercept of two isopleths (point A; Fig. 10b), which determines dT/dt at 10^{-4} °C/yr•mm^2 and T_0 at 1100 °C. If samples have identical T_{Mg} and T_{REE} (e.g., point B in Fig. 10b), T_{Mg} and T_{REE} could only tell T_0 and the lower limits of dT/dt; if samples reach the upper boundary (e.g., point C in Fig. 10b), T_{Mg} and T_{REE} can only constrain dT/dt and the lower limits of T_0. However, samples may also go beyond the upper limit or below the zero-horizontal line in Fig. 10b, as a result of inaccurate estimations of closure temperatures or complex thermal histories; for these samples, no solutions can be obtained from this two element-coupled geospeedometer.

The aforementioned inversion approach is based on the numerical simulations of Mg and REE diffusion for a plagioclase-clinopyroxene aggregate with a specified grain radius, mineral mode and plagioclase composition. Given that natural mafic cumulate samples likely have a wide range of grain sizes, mineral modes, and plagioclase compositions, a substantial amount of numerical simulations are thus needed to establish the exact expressions of T_{Mg} and T_{REE} and to further invert dT/dt and T_0 for individual samples. For convenience, Sun and Lissenberg (2018a) compiled their numerical solutions from 1.575×10^5 diffusion simulations in a multi-dimensional grid that can be used to interpolate the expressions of T_{Mg} and T_{REE} for a wide range of plagioclase compositions, mineral proportions, and grain radii. Using the Matlab® program provided in Sun and Lissenberg (2018a), interested users could readily automate the inverse calculations of T_0 and dT/dt for a batch of mafic cumulate samples.

5. A case study on oceanic crust formation

The cumulate section of oceanic crust is mainly composed of gabbros and gabbronorites that solidifies from mantle-derived magmas beneath the spreading mid-ocean ridges. Among the existing models for oceanic crust formation at fast spreading mid-ocean ridges, two end-members remain debating on whether oceanic cumulates crystalize mainly in a shallow melt lens (e.g., Sleep, 1978; Phipps Morgan & Chen, 1993; Quick & Denlinger, 1993; Coogan et al., 2007; Faak et al., 2015) or largely in situ from various magma sills in the lower crust (e.g., Nicolas et al., 1988; Kelemen et al., 1997;

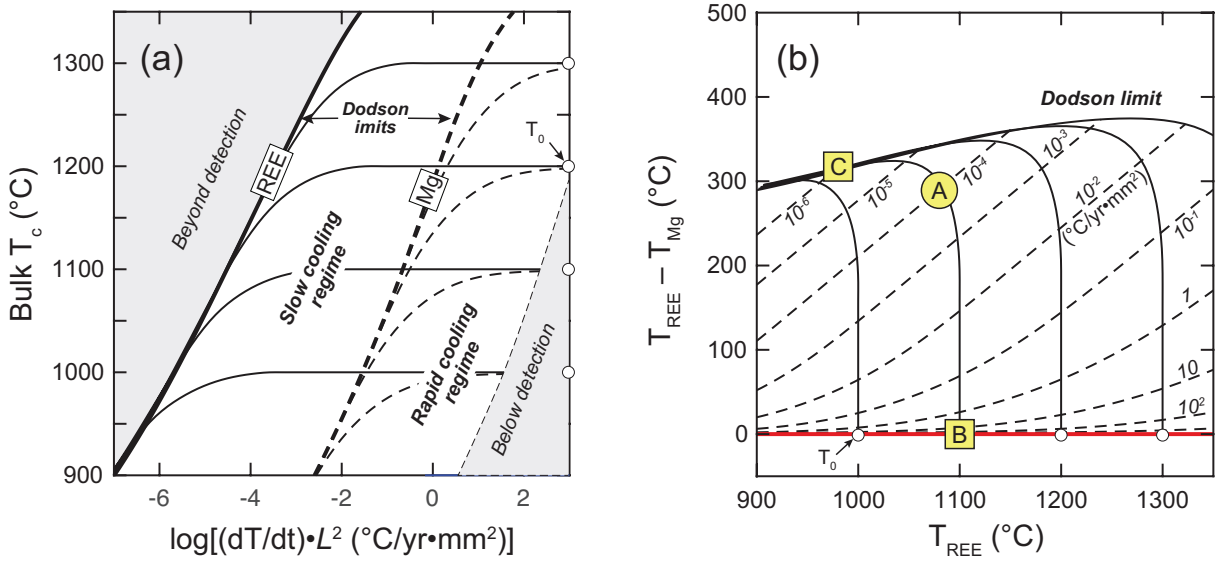

Figure 10. Numerical simulation results of REE (T_{REE}) and Mg (T_{Mg}) bulk closure temperatures for a plagioclase–clinopyroxene assemblage with a uniform grain radius and equal mineral mode (Sun & Lissenberg, 2018a). Plot (**a**) shows T_{REE} (solid curves) and T_{Mg} (dashed curves) as functions of effective cooling rates and initial temperatures, and plot (**b**) illustrates the simultaneous inversion of the cooling rate (dT/dt) and initial temperature (T_0) for a given sample by intercepting the two isopleths (dashed and solid curves for dT/dt and T_0, respectively). Given the observed compositional dependences (Cherniak, 2003; Faak et al., 2013; Van Orman et al., 2014; Sun & Liang, 2017; Sun & Lissenberg, 2018a), the diffusion and partition coefficients of REE and Mg in plagioclase need be calculated for different anorthite contents. The simulation here used plagioclase An$_{65}$.

Lissenberg et al., 2004; Maclennan et al., 2005; VanTongeren et al., 2008, 2015; Natland & Dick, 2009). The former implies that oceanic cumulates underwent near-conductive cooling in the deeper crust; however, the latter suggests that oceanic cumulates experienced rapid cooling perhaps due to crustal-scale hydrothermal circulations. Hence, these two models are differentiable by the cooling histories recorded in oceanic cumulate rocks.

The oceanic crust at Hess Deep rift valley is a reference section for fast-spreading oceanic crust and has been mapped and sampled in several previous studies (e.g., Karson et al., 2002; Lissenberg et al., 2013). Recently, a suite of gabbroic samples from Hess Deep have been reported with mineral compositions, detailed petrographic descriptions, and reconstructed stratigraphy (Lissenberg et al., 2013). Through dedicated analysis on representative samples, Sun and Lissenberg (2018a) further confirmed the reliability of MgO data in plagioclase from Lissenberg et al. (2013). To correct for the effects of grain size, Sun and Lissenberg (2018a) also measured the average grain sizes of plagioclase and clinopyroxene from these samples. This provides a total of 46 well-characterized samples from a reconstructed section of 4.35 km below the dike-gabbro transition (DGT) at Hess Deep. Among them, only 15 samples have REE data. However, the 15 samples define a strong positive linear relationship between the calculated REE closure temperatures and plagioclase An# (Fig. 6a), which can be used to empirically estimate the REE closure temperatures of other Hess Deep samples.

Applying the Mg–REE coupled geospeedometry (Section 4.3) to the Hess Deep samples, Sun and Lissenberg (2018a) successfully calculated the initial temperatures and cooling rates for 44 of the 46 samples. The inverted initial temperatures (998–1353 °C) are slightly greater than T_{REE} (998–1294 °C), but the overall differences are small, indicating small extents of diffusive re-distribution of REE in Hess Deep gabbros. As shown in Fig. 11a, near the DGT, the initial temperatures (998–1125 °C) vary over ~130 °C within 56 m, which suggests that the axial magma chamber is likely dominated by continuous influx and fractional crystallization of evolved melts from the deeper crust. The highly evolved temperatures near the DGT are consistent with the petrological evidence on Hess Deep samples (Natland & Dick, 1996). Although with the largest uncertainty (± 60 °C), the highest temperature (1353 °C) at 3523 m is comparable with the primary melt temperatures at mid-ocean ridges (1300–1400◦C; e.g., Lee et al., 2009). Similar temperatures (1261–1289 °C) also arise at 2066–3568 m, indicating emplacement of mantle-derived partial melts at various depths of the lower oceanic crust. The overall upward decrease of initial temperatures along the stratigraphy (Fig. 11a) suggests that the deeper crustal section (>2000 m) likely confines the overall temperatures of migrating melts in crystal mushes. Given the small-scale temperature variations in the deeper section, accumulation and in situ solidification of replenished melts likely proceed in small magma bodies at various depths, perhaps about tens to hundreds of meters in thickness, which is also supported by a recent magnetic anisotropy study (Morris et al., 2019).

Notably, the inverted cooling rates agree well with the cooling rates inferred from the hydrothermal cooling models of Maclennan et al. (2005) and are generally greater than those from Maclennan et al.'s conductive cooling model by about one to two orders of magnitude (Fig. 11b). This supports the previous notion of deep hydrothermal cooling of the lower oceanic crust (e.g., Maclennan et al., 2005; VanTongeren et al., 2008) and also appears to be compatible with the estimated

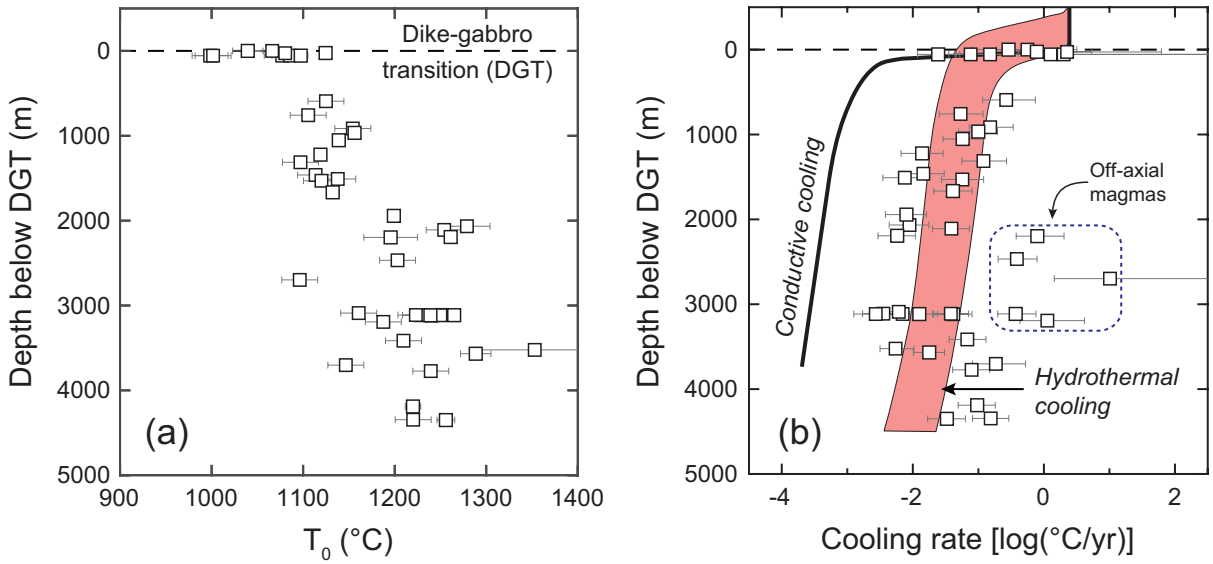

Figure 11. Stratigraphic variations of (**a**) the initial temperatures (T_0) and (**b**) cooling rates (dT/dt) derived from the Mg–REE coupled geospeedometer for the Hess Deep gabbros (Sun & Lissenberg, 2018a). Modeling results of Maclennan et al. (2005) for two different thermal models (conductive vs. hydrothermal) are shown in (**b**) for comparison with the inverted cooling rates.

cooling profiles of the upper most mantle section in Oman ophiolite (Dygert et al., 2017). More importantly, with a comprehensive coverage on the oceanic crust profile, the cooling rate results enable a systematic assessment of stratigraphic variations. Near the DGT, the inverted cooling rates vary over two orders of magnitude (0.024–2.26 °C/yr) within about 56 m, indicating efficient heat extraction at the axial magma chamber. The 5 samples at 2198–3193 m appear to have anomalously rapid cooling rates (0.372–10.2 °C/yr), indicative of more efficient heat extraction at localized regions of the lower oceanic crust. Such rapid cooling zones can be attributed to high hydrothermal flows at regional depths and/or to later intrusion of magma bodies into colder off-axial regions. Both mechanisms likely involve brittle-ductile transition in the lower oceanic crust. However, the latter appears to be favored by recent seismic observations at East Pacific Rise (e.g., Canales et al., 2012; Han et al., 2014). In addition, most of the high temperature samples (T_0 > 1260 °C; about 2066–3568 m) show relatively slow cooling rates (≤ 0.01 °C/yr) and thus solidified at extended time intervals that are consistent with multiple replenishments of mantle melts in the deeper crustal section.

The geospeedometry results of Hess Deep samples, together with previous evidence in petrology and seismology, lead Sun and Lissenberg (2018a) towards a new model for oceanic crust formation at fast-spreading mid-ocean ridges (see their Fig. 7). They suggested that the crust formation zone consists of a crustal-scale magma mush, off-axial magma bodies, and a shallow axial magma lens. According to the thermal structure from Dunn et al. (2000), the mush region may extend to ~1.5–3.5 km off the ridge axis, which is mainly constrained by crustal-scale hydrothermal circulations and mantle melt influx. As suggested by recent observations at Oman ophiolite (Zihlmann et al., 2018), the deep circulations of hydrothermal fluids may involve off-axial faulting in the lower crust. The replenished melts likely transport reactively through the mush and partly accumulate as small magma bodies at various depths. In situ crystallization and replenishment of these magma bodies can disturb the stratigraphic variations of crystallization temperatures and cooling rates recorded in the cumulate rocks. Along the brittle-ductile transition, melts may escape from the mush zone and segregate in the off-axial region. These off-axial magma bodies, if no successive melt influx, likely solidify on timescales of hundreds to thousands of years (see equation (52a)), according to the calculated cooling rates and crystallization temperatures (Fig. 11). However, the shallow axial magma lens is dynamically stable during crustal formation because of the continuous melt replenishment from the deeper mush zone.

6. Concluding remarks

The general framework of trace element-based geothermometry and geospeedometry was outlined in this paper and discussed with the recently developed geothermometers and geospeedometer for mafic cumulate rocks. I emphasized that trace elements, with relatively simple behaviors of partitioning and diffusion, have unique advantages over major elements for constructing new geothermometers and geospeedometers. Through lattice strain analyses of trace element partitioning, I showed that two-mineral exchange geothermometers can be calibrated using crystal-melt partitioning data for individual minerals. In particular, the lattice strain model also enables a new approach of geothermometer calibration by making use of the systematic partitioning behaviors of multiple trace elements with the same valent state (e.g., REE^{3+}), but before application to natural rocks, independent tests of the geothermometers are strongly required.

Although designed to determine the equilibrium temperatures, geothermometers can only decode closure temperatures from the natural mineral records. Due to cooling after the rock formation, mineral compositions have been reset to various extents by diffusive exchange with the surroundings. As shown by the Mg and REE thermometry of oceanic gabbros, such diffusive resetting mainly depends on the diffusion coefficients and leads the closure temperatures to deviate from the initial temperatures. Thus, the meaning of thermometer-determined closure temperatures has to be interpreted using relevant geospeedometers in the context of cooling histories, i.e., cooling rates and initial temperatures. These two cooling parameters are equally important for understanding the thermal histories of a rock system but are challenging to constrain together. However, the differential diffusive responses of two elements with distinct geochemical behaviors provides a general resolution to this problem by combining the closure temperatures (or profiles) of two or multiple geochemically distinct elements in the same petrological system.

As an example, I showed that coupling Mg and REE diffusive closures in plagioclase-clinopyroxene systems can be used to simultaneously determine the crystallization temperatures and cooling rates of mafic cumulate rocks. Coupled with stratigraphic information, the speedometry results enable one to establish a comprehensive record of igneous accretion and cooling styles during igneous crust formation, which was demonstrated by the case study on Hess Deep gabbros from the fast-spreading East Pacific Rise. This Mg-REE coupled geospeedometer could be applied to mafic cumulate rocks from other geological settings, such as slow-spreading ridges and ophiolites, for comparative studies on the formation and thermal structures of oceanic crusts. In addition, it could also be used to delineate the first-order information on crustal formation at other rocky planetary bodies (e.g., Moon, Vesta, and Mars) through returned samples or meteorites despite the lack of geological contexts.

Acknowledgements

Many collaborators and colleagues have inspired the author's interests in trace element partitioning, geothermobarometry, geospeedometry, ocean ridge processes, and experimental petrology in general over the years,

including in particular Yan Liang, Bruce Watson, Nobu Shimizu, Henry Dick, Johan Lissenberg, Lijing Yao, Cin-Ty Lee, and Rajdeep Dasgupta. Detailed comments from Flavio Di Stefano and an anonymous reviewer helped the author improve the presentation of this paper and are greatly appreciated. The author was also grateful to Matteo Masotta and Silvio Mollo for their editorial advices. The geospeedometry work was supported by Devonshire postdoctoral scholarship at WHOI and NSF grant OCE-1637130.

References

Anders, E., & Grevesse, N. (1989). Abundances of the elements: Meteoritic and solar. *Geochimica et Cosmochimica Acta*, *53*(1), 197–214. https://doi.org/10.1016/0016-7037(89)90286-X

Ashwal, L. D., Webb, S. J., & Knoper, M. W. (2005). Magmatic stratigraphy in the Bushveld Northern Lobe: Continuous geophysical and mineralogical data from the 2950 m Bellevue drillcore. *South African Journal of Geology*, *108*(2), 199–232. https://doi.org/10.2113/108.2.199

Bachmann, O., & Bergantz, G. W. (2004). On the origin of crystal-poor rhyolites: Extracted from batholithic crystal mushes. *Journal of Petrology*, *45*(8), 1565–1582. https://doi.org/10.1093/petrology/egh019

Bachmann, O., & Huber, C. (2016). Silicic magma reservoirs in the Earth's crust. *American Mineralogist*, Vol. 101, pp. 2377–2404. https://doi.org/10.2138/am-2016-5675

Blundy, J., & Wood, B. (1994). Prediction of crystal-melt partition coefficients from elastic moduli. *Nature*, *372*(6505), 452–454. https://doi.org/10.1038/372452a0

Bohrson, W. A., Spera, F. J., Ghiorso, M. S., Brown, G. A., Creamer, J. B., & Mayfield, A. (2014). Thermodynamic model for energy-constrained open-system evolution of crustal magma bodies undergoing simultaneous recharge, assimilation and crystallization: The magma chamber simulator. *Journal of Petrology*, *55*(9), 1685–1717. https://doi.org/10.1093/petrology/egu036

Brady, J. B., & McCallister, R. H. (1983). Diffusion data for clinopyroxenes from homogenization and self-diffusion experiments. *American Mineralogist*, *68*, 95–105. Retrieved from http://www.minsocam.org/ammin/AM68/AM68_95.pdf

Brice, J. C. (1975). Some thermodynamic aspects of the growth of strained crystals. *Journal of Crystal Growth*, *28*(2), 249–253. https://doi.org/10.1016/0022-0248(75)90241-9

Canales, J. P., Carton, H., Carbotte, S. M., Mutter, J. C., Nedimović, M. R., Xu, M., … Newman, K. (2012). Network of off-axis melt bodies at the East Pacific Rise. *Nature Geoscience*, *5*(4), 279–283. https://doi.org/10.1038/ngeo1377

Cawthorn, R. G., & Walraven, F. (1998). Emplacement and crystallization time for the Bushveld Complex. *Journal of Petrology*, *39*(9), 1669–1687. https://doi.org/10.1093/petroj/39.9.1669

Chakraborty, S. (1997). Rates and mechanisms of Fe-Mg interdiffusion in olivine at 980°-1300°C. *Journal of Geophysical Research: Solid Earth*, *102*(B6), 12317–12331. https://doi.org/10.1029/97jb00208

Cherniak, D. J. (2003). REE diffusion in feldspar. *Chemical Geology*, *193*(1–2), 25–41. https://doi.org/10.1016/S0009-2541(02)00246-2

Cherniak, D. J., & Dimanov, A. (2010). Diffusion in Pyroxene, Mica and Amphibole. *Reviews in Mineralogy and Geochemistry*, *72*(1), 641–690. https://doi.org/10.2138/rmg.2010.72.14

Coogan, L. A., Jenkin, G. R. T., & Wilson, R. N. (2007). Contrasting cooling rates in the lower oceanic crust at fast- and slow-spreading ridges revealed by geospeedometry. *Journal of Petrology*, *48*(11), 2211–2231. https://doi.org/10.1093/petrology/egm057

Costa, F., Chakraborty, S., & Dohmen, R. (2003). Diffusion coupling between trace and major elements and a model for calculation of magma residence times using plagioclase. *Geochimica et Cosmochimica Acta*, *67*(12), 2189–2200. https://doi.org/10.1016/S0016-7037(02)01345-5

Costa, F., & Dungan, M. (2005). Short time scales of magmatic assimilation from diffusion modeling of multiple elements in olivine. *Geology*, *33*(10), 837–840. https://doi.org/10.1130/G21675.1

Darken, L. S. (1948). Diffusion, mobility and their interrelation through free energy in binary metallic systems. *Transactions of the Metallurgical Society of AIME*, *175*, 184–201. https://doi.org/10.1007/s11661-010-0177-7

DePaolo, D. J. (1981). Trace element and isotopic effects of combined wallrock assimilation and fractional crystallization. *Earth and Planetary Science Letters*, *53*(2), 189–202. https://doi.org/10.1016/0012-821X(81)90153-9

DePaolo, D. J. (1985). Isotopic studies of processes in mafic magma chambers: I. The kiglapait intrusion, labrador. *Journal of Petrology*, *26*(4), 925–951. https://doi.org/10.1093/petrology/26.4.925

Dodson, M. H. (1973). Closure temperature in cooling geochronological and petrological systems. *Contributions to Mineralogy and Petrology*, *40*(3), 259–274. https://doi.org/10.1007/BF00373790

Dodson, M. H. (1986). Closure Profiles in Cooling Systems. *Materials Science Forum*, *7*, 145–154. https://doi.org/10.4028/www.scientific.net/msf.7.145

Dunn, R. A., Toomey, D. R., & Solomon, S. C. (2000). Three-dimensional seismic structure and physical properties of the crust and shallow mantle beneath the East Pacific Rise at 9°30'N. *Journal of Geophysical Research: Solid Earth*, *105*(B10), 23537–23555. https://doi.org/10.1029/2000jb900210

Dygert, N., Kelemen, P. B., & Liang, Y. (2017). Spatial variations in cooling rate in the mantle section of the Samail ophiolite in Oman: Implications for formation of lithosphere at mid-ocean ridges. *Earth and Planetary Science Letters*, *465*, 134–144. https://doi.org/10.1016/j.epsl.2017.02.038

Edmonds, M., Cashman, K. V., Holness, M., & Jackson, M. (2019). Architecture and dynamics of magma reservoirs. *Philosophical Transactions of the Royal Society A: Mathematical, Physical and Engineering Sciences*, Vol. 377. https://doi.org/10.1098/rsta.2018.0298

Ehlers, K., & Powell, R. (1994). An empirical modification of Dodson's equation for closure temperature in binary systems. *Geochimica et Cosmochimica Acta*, *58*(1), 241–

248. https://doi.org/10.1016/0016-7037(94)90461-8

Eiler, J. M., Baumgartner, L. P., & Valley, J. W. (1992). Intercrystalline stable isotope diffusion: a fast grain boundary model. *Contributions to Mineralogy and Petrology*, *112*(4), 543–557. https://doi.org/10.1007/BF00310783

Ellis, D. J., & Green, D. H. (1979). An experimental study of the effect of Ca upon garnet-clinopyroxene Fe-Mg exchange equilibria. *Contributions to Mineralogy and Petrology*, *71*(1), 13–22. https://doi.org/10.1007/BF00371878

Faak, K., Chakraborty, S., & Coogan, L. A. (2013). Mg in plagioclase: Experimental calibration of a new geothermometer and diffusion coefficients. *Geochimica et Cosmochimica Acta*, *123*, 195–217. https://doi.org/10.1016/j.gca.2013.05.009

Faak, K., Coogan, L. A., & Chakraborty, S. (2015). Near conductive cooling rates in the upper-plutonic section of crust formed at the East Pacific Rise. *Earth and Planetary Science Letters*, *423*, 36–47. https://doi.org/10.1016/j.epsl.2015.04.025

Feig, S. T., Koepke, J., & Snow, J. E. (2006). Effect of water on tholeiitic basalt phase equilibria: An experimental study under oxidizing conditions. *Contributions to Mineralogy and Petrology*, *152*(5), 611–638. https://doi.org/10.1007/s00410-006-0123-2

Gaetani, G. A., & Grove, T. L. (1995). Partitioning of rare earth elements between clinopyroxene and silicate melt Crystal-chemical controls. *Geochimica et Cosmochimica Acta*, *59*(10), 1951–1962. https://doi.org/10.1016/0016-7037(95)00119-0

Ganguly, J., & Tirone, M. (1999). Diffusion closure temperature and age of a mineral with arbitrary extent of diffusion: Theoretical formulation and applications. *Earth and Planetary Science Letters*, *170*(1–2), 131–140. https://doi.org/10.1016/S0012-821X(99)00089-8

Green, T. H., & Ringwood, A. E. (1968). Genesis of the calc-alkaline igneous rock suite. *Contributions to Mineralogy and Petrology*, *18*(2), 105–162. https://doi.org/10.1007/BF00371806

Grove, T. L., & Bryan, W. B. (1983). Fractionation of pyroxene-phyric MORB at low pressure: An experimental study. *Contributions to Mineralogy and Petrology*, *84*(4), 293–309. https://doi.org/10.1007/BF01160283

Grove, T. L., Elkins-Tanton, L. T., Parman, S. W., Chatterjee, N., Müntener, O., & Gaetani, G. A. (2003). Fractional crystallization and mantle-melting controls on calc-alkaline differentiation trends. *Contributions to Mineralogy and Petrology*, *145*(5), 515–533. https://doi.org/10.1007/s00410-003-0448-z

Grove, T. L., Gerlach, D. C., & Sando, T. W. (1982). Origin of calc-alkaline series lavas at Medicine Lake Volcano by fractionation, assimilation and mixing. *Contributions to Mineralogy and Petrology*, *80*(2), 160–182. https://doi.org/10.1007/BF00374893

Han, S., Carbotte, S. M., Carton, H., Mutter, J. C., Aghaei, O., Nedimović, M. R., & Canales, J. P. (2014). Architecture of on- and off-axis magma bodies at EPR 9°37-40'N and implications for oceanic crustal accretion. *Earth and Planetary Science Letters*, *390*, 31–44. https://doi.org/10.1016/j.epsl.2013.12.040

Hildreth, W. (1979). The Bishop Tuff: Evidence for the origin of compositional zonation in silicic magma chambers. *Geological Society of America Special Paper*, *180*, 43–76. https://doi.org/10.1130/spe180-p43

Karson, J. A., Klein, E. M., Hurst, S. D., Lee, C. E., Rivizzigno, P. A., Curewitz, D., … Sutton, A. L. (2002). Structure of uppermost fast-spread oceanic crust exposed at the Hess Deep Rift: Implications for subaxial processes at the East Pacific Rise. *Geochemistry, Geophysics, Geosystems*, *3*. https://doi.org/10.1029/ 2001GC000155

Kelemen, P. B., Koga, K., & Shimizu, N. (1997). Geochemistry of gabbro sills in the crust-mantle transition zone of the Oman ophiolite: implications for the origin of the oceanic lower crust. *Earth and Planetary Science Letters*, *146*(3–4), 475–488. https://doi.org/10.1016/S0012-821X(96)00235-X

Koepke, J., Botcharnikov, R. E., & Natland, J. H. (2018). Crystallization of late-stage MORB under varying water activities and redox conditions: Implications for the formation of highly evolved lavas and oxide gabbro in the ocean crust. *Lithos*, *323*, 58–77. https://doi.org/10.1016/j.lithos.2018.10.001

Kruger, F. J. (2005). Filling the Bushveld Complex magma chamber: Lateral expansion, roof and floor interaction, magmatic unconformities, and the formation of giant chromitite, PGE and Ti-V-magnetitite deposits. *Mineralium Deposita*, *40*(5), 451–472. https://doi.org/10.1007/s00126-005-0016-8

Lasaga, A. C. (1979). Multicomponent exchange and diffusion in silicates. *Geochimica et Cosmochimica Acta*, *43*(4), 455–469. https://doi.org/10.1016/0016-7037(79)90158-3

Lasaga, A. C. (1983). Geospeedometry: An Extension of Geothermometry. In *Kinetics and equilibrium in mineral reactions* (pp. 81–114). https://doi.org/10.1007/978-1-4612-5587-1_3

Lasaga, A. C., Richardson, S. M., & Holland, H. D. (1977). The Mathematics of Cation Diffusion and Exchange Between Silicate Minerals During Retrograde Metamorphism. In *Energetics of Geological Processes* (pp. 353–388). https://doi.org/10.1007/978-3-642-86574-9_15

Le Roux, V., Dasgupta, R., & Lee, C. T. A. (2011). Mineralogical heterogeneities in the Earth's mantle: Constraints from Mn, Co, Ni and Zn partitioning during partial melting. *Earth and Planetary Science Letters*, *307*(3–4), 395–408. https://doi.org/10.1016/j.epsl.2011.05.014

Lee, C.-T. A., Harbert, A., & Leeman, W. P. (2007). Extension of lattice strain theory to mineral/mineral rare-earth element partitioning: An approach for assessing disequilibrium and developing internally consistent partition coefficients between olivine, orthopyroxene, clinopyroxene and basaltic melt. *Geochimica et Cosmochimica Acta*, *71*(2), 481–496. https://doi.org/10.1016/j.gca.2006.09.014

Lee, C.-T. A., Lee, T. C., & Wu, C. T. (2014). Modeling the compositional evolution of recharging, evacuating, and fractionating (REFC) magma chambers: Implications for differentiation of arc magmas. *Geochimica et Cosmochimica Acta*, *143*, 8–22. https://doi.org/10.1016/j.gca.2013.08.009

Liang, Y. (2010). Multicomponent Diffusion in Molten Silicates: Theory, Experiments, and Geological Applications. *Reviews in Mineralogy and Geochemistry*, *72*(1), 409–446. https://doi.org/10.2138/rmg.2010.72.9

Liang, Y. (2015). A simple model for closure temperature of a trace element in cooling bi-mineralic systems. *Geochimica et Cosmochimica Acta*, *165*, 35–43. https://doi.org/10.1016/j.gca.2015.05.028

Liang, Y., Sun, C., & Yao, L. (2013). A REE-in-two-pyroxene thermometer for mafic and ultramafic rocks. *Geochimica et Cosmochimica Acta*. https://doi.org/10.1016/j.gca.2012.10.035

Lissenberg, C. J., Bédard, J. H., & van Staal, C. R. (2004). The structure and geochemistry of the gabbro zone of the Annieopsquotch ophiolite, Newfoundland: Implications for lower crustal accretion at spreading ridges. *Earth and Planetary Science Letters*, *229*(1–2), 105–123. https://doi.org/10.1016/j.epsl.2004.10.029

Lissenberg, C. J., MacLeod, C. J., Howard, K. A., & Godard, M. (2013). Pervasive reactive melt migration through fast-spreading lower oceanic crust (Hess Deep, equatorial Pacific Ocean). *Earth and Planetary Science Letters*, *361*, 436–447. https://doi.org/10.1016/j.epsl.2012.11.012

Maclennan, J. (2019). Mafic tiers and transient mushes: Evidence from Iceland. *Philosophical Transactions of the Royal Society A: Mathematical, Physical and Engineering Sciences*, Vol. 377. https://doi.org/10.1098/rsta.2018.0021

Maclennan, J., Hulme, T., & Singh, S. C. (2005). Cooling of the lower oceanic crust. *Geology*, *33*(5), 357–360. https://doi.org/10.1130/G21207.1

Masotta, M., Mollo, S., Freda, C., Gaeta, M., & Moore, G. (2013). Clinopyroxene-liquid thermometers and barometers specific to alkaline differentiated magmas. *Contributions to Mineralogy and Petrology*, *166*(6), 1545–1561. https://doi.org/10.1007/s00410-013-0927-9

McBirney, A. R. (2003). The Skaergaard Layered Series, Part VII: Sr and Nd Isotopes. *Journal of Petrology*, *44*(4), 757–771. https://doi.org/10.1093/petrology/44.4.757

Mollo, S., Blundy, J., Scarlato, P., De Cristofaro, S. P., Tecchiato, V., Di Stefano, F., … Bachmann, O. (2018). An integrated P-T-H2O-lattice strain model to quantify the role of clinopyroxene fractionation on REE+Y and HFSE patterns of mafic alkaline magmas: Application to eruptions at Mt. Etna. *Earth-Science Reviews*, Vol. 185, pp. 32–56. https://doi.org/10.1016/j.earscirev.2018.05.014

Mollo, S., Putirka, K., Iezzi, G., Del Gaudio, P., & Scarlato, P. (2011). Plagioclase-melt (dis)equilibrium due to cooling dynamics: Implications for thermometry, barometry and hygrometry. *Lithos*, *125*(1–2), 221–235. https://doi.org/10.1016/j.lithos.2011.02.008

Morgan, D. J., & Blake, S. (2006). Magmatic residence times of zoned phenocrysts: Introduction and application of the binary element diffusion modelling (BEDM) technique. *Contributions to Mineralogy and Petrology*, *151*(1), 58–70. https://doi.org/10.1007/s00410-005-0045-4

Morris, A., Meyer, M., Anderson, M. W., & MacLeod, C. J. (2019). What do variable magnetic fabrics in gabbros of the Oman ophiolite reveal about lower oceanic crustal magmatism at fast spreading ridges? *Geology*, *47*(3), 275–278. https://doi.org/10.1130/G45442.1

Morse, S. A., Brady, J. B., & Sporleder, B. A. (2004). Experimental petrology of the Kiglapait Intrusion: Cotectic trace for the Lower Zone at 5 kbar in graphite. *Journal of Petrology*, *45*(11), 2225–2259. https://doi.org/10.1093/petrology/egh054

Müller, T., Dohmen, R., Becker, H. W., ter Heege, J. H., & Chakraborty, S. (2013). Fe-Mg interdiffusion rates in clinopyroxene: Experimental data and implications for Fe-Mg exchange geothermometers. *Contributions to Mineralogy and Petrology*, *166*(6), 1563–1576. https://doi.org/10.1007/s00410-013-0941-y

Namur, O., & Humphreys, M. C. S. (2018). Trace element constraints on the differentiation and crystal mush solidification in the Skaergaard intrusion, Greenland. *Journal of Petrology*, *59*(3), 387–418. https://doi.org/10.1093/petrology/egy032

Natland, J. H., & Dick, H. J. B. (1996). Melt Migration through High-Level Gabbroic Cumulates of the East Pacific Rise at Hess Deep: The Origin of Magma Lenses and the Deep Crustal Structure of Fast-Spreading Ridges. *Proceedings of the Ocean Drilling Program, 147 Scientific Results*, 21–58. https://doi.org/10.2973/odp.proc.sr.147.002.1996

Natland, J. H., & Dick, H. J. B. (2009). Paired melt lenses at the East Pacific Rise and the pattern of melt flow through the gabbroic layer at a fast-spreading ridge. *Lithos*, *112*(1–2), 73–86. https://doi.org/10.1016/j.lithos.2009.06.017

Nicolas, A., Reuber, I., & Benn, K. (1988). A new magma chamber model based on structural studies in the Oman ophiolite. *Tectonophysics*, *151*(1–4), 87–105. https://doi.org/10.1016/0040-1951(88)90242-9

O'Neill, H. S. C., & Wood, B. J. (1979). An experimental study of Fe-Mg partitioning between garnet and olivine and its calibration as a geothermometer. *Contributions to Mineralogy and Petrology*, *70*(1), 59–70. https://doi.org/10.1007/BF00371872

Onuma, N., Higuchi, H., Wakita, H., & Nagasawa, H. (1968). Trace element partition between two pyroxenes and the host lava. *Earth and Planetary Science Letters*, *5*, 47–51. https://doi.org/10.1016/s0012-821x(68)80010-x

Phipps Morgan, J., & Chen, Y. J. (1993). The genesis of oceanic crust: Magma injection, hydrothermal circulation, and crustal flow. *Journal of Geophysical Research: Solid Earth*, *98*(B4), 6283–6297. https://doi.org/10.1029/92jb02650

Putirka, K. D. (2005). Igneous thermometers and barometers based on plagioclase + liquid equilibria: Tests of some existing models and new calibrations. *American Mineralogist*, Vol. 90, pp. 336–346. https://doi.org/10.2138/am.2005.1449

Putirka, K. D. (2008). Thermometers and barometers for volcanic systems. *Reviews in Mineralogy and Geochemistry*, *69*, 61–120. https://doi.org/10.2138/rmg.2008.69.3

Quick, J. E., & Denlinger, R. P. (1993). Ductile deformation and the origin of layered gabbro in ophiolites. *Journal of Geophysical Research: Solid Earth*, *98*(B8), 14015–14027. https://doi.org/10.1029/93jb00698

Sack, R. O., Walker, D., & Carmichael, I. S. E. (1987). Experimental petrology of alkalic lavas: constraints on cotectics of multiple saturation in natural basic liquids. *Contributions to Mineralogy and Petrology*, *96*(1), 1–23. https://doi.org/10.1007/BF00375521

Shannon, R. D. (1976). Revised effective ionic radii and systematic studies of interatomic distances in halides and chalcogenides. *Acta Crystallographica Section A*, *32*, 751–767.

Sisson, T. W., & Grove, T. L. (1993). Experimental investigations of the role of H2O in calc-alkaline differentiation and subduction zone magmatism. *Contributions to Mineralogy and Petrology*, *113*(2), 143–166. https://doi.org/10.1007/BF00283225

Sleep, N. H. (1978). Thermal structure and kinematics of mid-oceanic ridge axis, some implications to basaltic volcanism. *Geophysical Research Letters*, *5*(6), 426–428. https://doi.org/10.1029/GL005i006p00426

Spera, F. J., & Bohrson, W. A. (2004). Open-system magma chamber evolution: An energy-constrained geochemical model incorporating the effects of concurrent eruption, recharge, variable assimilation and fractional crystallization (EC-E′RAχ FC). *Journal of Petrology*, *45*(12), 2459–2480. https://doi.org/10.1093/petrology/egh072

Sun, C. (2018). Partitioning and Partition Coefficients. In W. M. White (Ed.), *Encyclopedia of Geochemistry. Encyclopedia of Earth Sciences Series*. https://doi.org/10.1007/978-3-319-39193-9_347-1

Sun, C., Graff, M., & Liang, Y. (2017). Trace element partitioning between plagioclase and silicate melt: The importance of temperature and plagioclase composition, with implications for terrestrial and lunar magmatism. *Geochimica et Cosmochimica Acta*, *206*, 273–295. https://doi.org/10.1016/j.gca.2017.03.003

Sun, C., & Liang, Y. (2012). Distribution of REE between clinopyroxene and basaltic melt along a mantle adiabat: Effects of major element composition, water, and temperature. *Contributions to Mineralogy and Petrology*, *163*(5), 807–823. https://doi.org/10.1007/s00410-011-0700-x

Sun, C., & Liang, Y. (2013a). Distribution of REE and HFSE between low-Ca pyroxene and lunar picritic melts around multiple saturation points. *Geochimica et Cosmochimica Acta*, *119*, 340–358. https://doi.org/10.1016/j.gca.2013.05.036

Sun, C., & Liang, Y. (2013b). The importance of crystal chemistry on REE partitioning between mantle minerals (garnet, clinopyroxene, orthopyroxene, and olivine) and basaltic melts. *Chemical Geology*, *358*, 23–36. https://doi.org/10.1016/j.chemgeo.2013.08.045

Sun, C., & Liang, Y. (2014). An assessment of subsolidus re-equilibration on REE distribution among mantle minerals olivine, orthopyroxene, clinopyroxene, and garnet in peridotites. *Chemical Geology*, *372*, 80–91. https://doi.org/10.1016/j.chemgeo.2014.02.014

Sun, C., & Liang, Y. (2015). A REE-in-garnet-clinopyroxene thermobarometer for eclogites, granulites and garnet peridotites. *Chemical Geology*, *393–394*, 79–92. https://doi.org/10.1016/j.chemgeo.2014.11.014

Sun, C., & Liang, Y. (2017). A REE-in-plagioclase–clinopyroxene thermometer for crustal rocks. *Contributions to Mineralogy and Petrology*, *172*(4). https://doi.org/10.1007/s00410-016-1326-9

Sun, C., & Lissenberg, C. J. (2018a). Formation of fast-spreading lower oceanic crust as revealed by a new Mg–REE coupled geospeedometer. *Earth and Planetary Science Letters*, *487*, 165–178. https://doi.org/10.1016/j.epsl.2018.01.032

Sun, C., & Lissenberg, C. J. (2018b). Caveats and challenges in geospeedometry: A reply to Faak et al.'s critique of the Mg–REE coupled geospeedometry. *Earth and Planetary Science Letters*, *502*, 287–290. https://doi.org/10.1016/j.epsl.2018.08.044

Takagi, D., Sato, H., & Nakagawa, M. (2005). Experimental study of a low-alkali tholeiite at 1-5 kbar: Optimal condition for the crystallization of high-An plagioclase in hydrous arc tholeiite. *Contributions to Mineralogy and Petrology*, *149*(5), 527–540. https://doi.org/10.1007/s00410-005-0666-7

Tecchiato, V., Gaeta, M., Mollo, S., Bachmann, O., Quadt, A. Von, & Scarlato, P. (2018). Snapshots of primitive arc magma evolution recorded by clinopyroxene textural and compositional variations: The case of hybrid crystal-rich enclaves from Capo Marargiu Volcanic District (Sardinia, Italy). *American Mineralogist*, *103*(6), 899–910. https://doi.org/10.2138/am-2018-6446

Tegner, C., Thy, P., Holness, M. B., Jakobsen, J. K., & Lesher, C. E. (2009). Differentiation and compaction in the Skaergaard intrusion. *Journal of Petrology*, *50*(5), 813–840. https://doi.org/10.1093/petrology/egp020

Thy, P., Lesher, C. E., & Fram, M. S. (1998). Low pressure experimental constraints on the evolution of basaltic lavas from Site 917, southeast Greenland Continental Margin. *Proceedings of the Ocean Drilling Program: Scientific Results*, *152*, 359–372.

Tiepolo, M., Oberti, R., Zanetti, A., Vannucci, R., & Foley, S. F. (2007). Trace-Element Partitioning Between Amphibole and Silicate Melt. *Reviews in Mineralogy and Geochemistry*, *67*(1), 417–452. https://doi.org/10.2138/rmg.2007.67.11

Van Orman, J. A., Cherniak, D. J., & Kita, N. T. (2014). Magnesium diffusion in plagioclase: Dependence on composition, and implications for thermal resetting of the 26Al-26Mg early solar system chronometer. *Earth and Planetary Science Letters*, *385*, 79–88. https://doi.org/10.1016/j.epsl.2013.10.026

Van Orman, J. A., Grove, T. L., & Shimizu, N. (2001). Rare earth element diffusion in diopside: influence of temperature, pressure, and ionic radius, and an elastic model for diffusion in silicates. *Contributions to Mineralogy and Petrology*, *141*(6), 687–703. https://doi.org/10.1007/s004100100269

van Westrenen, W., & Draper, D. S. (2007). Quantifying garnet-melt trace element partitioning using lattice-strain theory: New crystal-chemical and thermodynamic constraints. *Contributions to Mineralogy and Petrology*, *154*(6), 717–730. https://doi.org/10.1007/s00410-007-0222-8

VanTongeren, J. A., Hirth, G., & Kelemen, P. B. (2015). Constraints on the accretion of the gabbroic lower oceanic crust from plagioclase lattice preferred orientation in the Samail ophiolite. *Earth and Planetary Science Letters*, *427*, 249–261. https://doi.org/10.1016/j.epsl.2015.07.001

VanTongeren, J. A., Kelemen, P. B., & Hanghøj, K. (2008). Cooling rates in the lower crust of the Oman ophiolite: Ca in olivine, revisited. *Earth and Planetary Science Letters*, *267*(1–2), 69–82. https://doi.org/10.1016/j.epsl.2007.11.034

VanTongeren, J. A., & Mathez, E. A. (2013). Incoming magma composition and style of recharge below the pyroxenite marker, eastern bushveld complex, south africa. *Journal of Petrology*, *54*(8), 1585–1605.

https://doi.org/10.1093/petrology/egt024
Veksler, I. V., Sedunova, A. P., Darin, A. V., Anosova, M. O., Reid, D. L., Kaufmann, F. E. D., … Trumbull, R. B. (2018). Chemical and textural re-equilibration in the UG2 chromitite layer of the Bushveld Complex, South Africa. *Journal of Petrology*, *59*(6), 1193–1216. https://doi.org/10.1093/petrology/egy058
Villiger, S., Ulmer, P., Müntener, O., & Thompson, A. B. (2004). The liquid line of descent of anhydrous, mantle-derived, tholeiitic liquids by fractional and equilibrium crystallization - An experimental study at 1·0 GPa. *Journal of Petrology*, *45*(12), 2369–2388. https://doi.org/10.1093/petrology/egh042
Wang, Z., Hiraga, T., & Kohlstedt, D. L. (2004). Effect of H+ on Fe–Mg interdiffusion in olivine, (Fe,Mg)2SiO4. *Applied Physics Letters*, *85*(2), 209–211. https://doi.org/10.1063/1.1769593
Wark, D. A., Hildreth, W., Spear, F. S., Cherniak, D. J., & Watson, E. B. (2007). Pre-eruption recharge of the Bishop magma system. *Geology*, *35*(3), 235–238. https://doi.org/10.1130/G23316A.1
Wark, D. A., & Watson, E. B. (2006). TitaniQ: A titanium-in-quartz geothermometer. *Contributions to Mineralogy and Petrology*, *152*(6), 743–754. https://doi.org/10.1007/s00410-006-0132-1
Waters, L. E., & Lange, R. A. (2015). An updated calibration of the plagioclase-liquid hygrometer-thermometer applicable to basalts through rhyolites. *American Mineralogist*, *100*(10), 2172–2184. https://doi.org/10.2138/am-2015-5232
Watson, E. B., & Baxter, E. F. (2007). Diffusion in solid-Earth systems. *Earth and Planetary Science Letters*, *253*(3–4), 307–327. https://doi.org/10.1016/j.epsl.2006.11.015
Watson, E. B., & Cherniak, D. J. (2015). Quantitative cooling histories from stranded diffusion profiles. *Contributions to Mineralogy and Petrology*, *169*(6). https://doi.org/10.1007/s00410-015-1153-4
Watson, E. B., & Harrison, T. M. (1984). Accessory minerals and the geochemical evolution of crustal magmatic systems: a summary and prospectus of experimental approaches. *Physics of the Earth and Planetary Interiors*, *35*(1–3), 19–30. https://doi.org/10.1016/0031-9201(84)90031-1
Watson, E. B., Wark, D. A., & Thomas, J. B. (2006). Crystallization thermometers for zircon and rutile. *Contributions to Mineralogy and Petrology*, *151*(4), 413–433. https://doi.org/10.1007/s00410-006-0068-5
Wood, B. J., & Blundy, J. D. (2013). Trace Element Partitioning: The Influences of Ionic Radius, Cation Charge, Pressure, and Temperature. In *Treatise on Geochemistry: Second Edition* (Vol. 3, pp. 421–448). https://doi.org/10.1016/B978-0-08-095975-7.00209-6
Yang, H.-J., Kinzler, R. J., & Grove, T. L. (1996). Experiments and models of anhydrous, basaltic olivine-plagioclase-augite saturated melts from 0.001 to 10 kbar. *Contributions to Mineralogy and Petrology*, *124*(1), 1–18. https://doi.org/10.1007/s004100050169
Yang, S. H., Maier, W. D., Godel, B., Barnes, S. J., Hanski, E., & O'Brien, H. (2019). Parental Magma Composition of the Main Zone of the Bushveld Complex: Evidence from in situ LA-ICP-MS Trace Element Analysis of Silicate Minerals in the Cumulate Rocks. *Journal of Petrology*, *60*(2), 359–392. https://doi.org/10.1093/petrology/egy115
Yao, L., & Liang, Y. (2015). Closure temperature in cooling bi-mineralic systems: I. Definition and with application to REE-in-two-pyroxene thermometer. *Geochimica et Cosmochimica Acta*, *162*, 137–150. https://doi.org/10.1016/j.gca.2015.03.041
Yao, L., Sun, C., & Liang, Y. (2012). A parameterized model for REE distribution between low-Ca pyroxene and basaltic melts with applications to REE partitioning in low-Ca pyroxene along a mantle adiabat and during pyroxenite-derived melt and peridotite interaction. *Contributions to Mineralogy and Petrology*, *164*(2), 261–280. https://doi.org/10.1007/s00410-012-0737-5
Zhang, X., Ganguly, J., & Ito, M. (2010). Ca-Mg diffusion in diopside: Tracer and chemical inter-diffusion coefficients. *Contributions to Mineralogy and Petrology*, *159*(2), 175–186. https://doi.org/10.1007/s00410-009-0422-5
Zhang, Y. (2010). Diffusion in Minerals and Melts: Theoretical Background. *Reviews in Mineralogy and Geochemistry*, *72*(1), 5–59. https://doi.org/10.2138/rmg.2010.72.2
Zihlmann, B., Müller, S., Coggon, R. M., Koepke, J., Garbe-Schönberg, D., & Teagle, D. A. H. (2018). Hydrothermal fault zones in the lower oceanic crust: An example from Wadi Gideah, Samail ophiolite, Oman. *Lithos*, *323*, 103–124. https://doi.org/10.1016/j.lithos.2018.09.008